JGR Oceans

RESEARCH ARTICLE
10.1029/2022JC018751

Upper-Ocean Turbulence Structure and Ocean-Ice Drag Coefficient Estimates Using an Ascending Microstructure Profiler During the MOSAiC Drift

Ilker Fer[1], Till M. Baumann[1], Zoé Koenig[1,2], Morven Muilwijk[1,2], and Sandra Tippenhauer[3]

[1]Geophysical Institute, University of Bergen, and Bjerknes Center for Climate Research, Bergen, Norway, [2]Norwegian Polar Institute, Tromsø, Norway, [3]Alfred Wegener Institute, Helmholtz Centre for Polar and Marine Research, Bremerhaven, Germany

Key Points:

- A novel ascending microstructure profiler successfully measured dissipation rates to within 1 m under the sea ice
- Dissipation rate estimates in the Arctic Ocean during the Multidisciplinary drifting Observatory for the Study of the Arctic Climate (MOSAiC) drift varied by more than four orders of magnitude
- A representative range of ice-ocean drag coefficient for the MOSAiC sampling site was (4–6) × 10^{-3}

Correspondence to:

I. Fer,
ilker.fer@uib.no

Citation:

Fer, I., Baumann, T. M., Koenig, Z., Muilwijk, M., & Tippenhauer, S. (2022). Upper-ocean turbulence structure and ocean-ice drag coefficient estimates using an ascending microstructure profiler during the MOSAiC drift. *Journal of Geophysical Research: Oceans*, *127*, e2022JC018751. https://doi.org/10.1029/2022JC018751

Received 15 APR 2022
Accepted 24 AUG 2022

Abstract Sea ice mediates the transfer of momentum, heat, and gas between the atmosphere and the ocean. However, the under-ice boundary layer is not sufficiently constrained by observations. During the Multidisciplinary drifting Observatory for the Study of the Arctic Climate (MOSAiC), we collected profiles in the upper 50–80 m using a new ascending vertical microstructure profiler, resolving the turbulent structure within 1 m to the ice. We analyzed 167 dissipation rate profiles collected between February and mid-September 2020, from 89°N to 79°30′N through the Amundsen Basin, Nansen Basin, Yermak Plateau, and Fram Strait. Measurements covered a broad range of forcing (0–15 m s^{-1} wind and 0–0.4 m s^{-1} drift speeds) and sea ice conditions (pack ice, thin ice, and leads). Dissipation rates varied by over 4 orders of magnitude from 10^{-9} W kg^{-1} below 40 m to above 10^{-5} W kg^{-1} at 1 m. Following wind events, layers with dissipation $\mathcal{O}(10^{-6})$ W kg^{-1} extended down to 20 m depth under pack ice. In leads in the central Arctic, turbulence was enhanced 2–10 times relative to thin ice profiles. Under-ice dissipation profiles allowed us to estimate the boundary layer thickness (4 ± 2 m), and the friction velocity (1–15 mm s^{-1}, 4.7 mm s^{-1} on average). A representative range of drag coefficient for the MOSAiC sampling site was estimated to (4–6) × 10^{-3}, which is a typical value for Arctic floe observations. The average ratio of drift speed to wind speed was close to the free-drift ratio of 2% with no clear seasonal or regional variability.

Plain Language Summary Turbulence in the ocean mixes water masses and redistributes heat, nutrients and dissolved gases. In the Arctic Ocean, the difference between the sea ice drift and the ocean currents below is a major source of turbulence. The turbulent layer under ice controls the exchange between ice and ocean. Unfortunately, conventional profiling instruments cannot measure turbulence within a few meters of the sea ice. Here we report on measurements collected during the Multidisciplinary drifting Observatory for the Study of the Arctic Climate (MOSAiC), using an instrument specially designed to profile upward from 50 to 80 m depth to the ice-water interface. We show that this instrument works satisfactorily in the Arctic conditions, delivering unique measurements of turbulence to within 1 m under ice. Measurements were taken in varying wind speed, ice drift, and sea ice conditions, and showed large variability. Energetic turbulent layers following wind events reached to 20 m depth under pack ice. In patches of open waters in the central Arctic, turbulence was more energetic compared to the profiles when the surface was covered by thin ice. Characteristic values that describe the exchange between the ice drift and turbulence are estimated and compared to earlier Arctic observations.

1. Introduction

The Arctic Ocean is partly covered by sea ice, with its extent changing seasonally from approximately 4 to 15 million km^2 from September to March (Meier et al., 2021). The presence and variability of this ice cover mediate the transfer of momentum, heat, matter, and gases between the atmosphere and ocean through several exchange processes. The long-term reduction trends in the extent, thickness, and age of the Arctic sea ice have become one of the most iconic indicators of global climate change (Meier et al., 2021). Thinner ice is more fractured with openings for air-sea exchange. The relative motion of sea ice and the ocean underneath sets up a shear. Shear stresses at the ice-ocean interface regulate the exchanges between the ocean and sea ice. In turn, the variability of sea ice over the Arctic Ocean is affected by the oceanic heat content and its turbulent transfer from the warm

waters below (Carmack et al., 2015; Lenn et al., 2021). A recent review of air-sea-ice interactions and processes in the under-ice boundary layer can be found in McPhee (2017).

Mixing in the Arctic Ocean drives water-mass transformations and affects the general Arctic circulation. Mixing rates may exceed the molecular levels by many orders of magnitude in turbulent conditions. In the ocean, turbulence is most commonly characterized by the viscous dissipation rate, ε, of turbulent kinetic energy (TKE), which tends to be the largest where forcing creates turbulence. In the upper ocean, turbulence is forced near the surface in open water or in the boundary layer under sea ice. The vertical structure beneath sea ice consists of a logarithmic boundary layer, typically a few meters thick, and a deeper Ekman layer, where the influence of the Earth's rotation becomes important (McPhee, 2008). Together, they are referred to as the under-ice boundary layer. In the logarithmic boundary layer, friction dominates and the stress is independent of depth (hence also called the frictional boundary layer or the constant-stress layer). In the following, we refer to this layer as the boundary layer. Turbulence under ice is typically generated through mechanical forcing by wind and shear stress and/or by buoyancy loss through brine rejection during sea-ice formation.

The vertical profile of ε is expected to vary substantially in the upper few meters, a region where the observations are very limited. The two most common methods of measuring ε are through measurements of turbulent fluctuations of velocity on ice-mounted systems at one or more fixed levels (1, 5 m below ice are typical, e.g., McPhee, 2008), or using tethered, free-falling vertical profilers equipped with shear probes (e.g., Fer, 2014). For reliable estimates of ε, the shear probes attached to profiling instruments require a steady, uncontaminated flow of water past sensors. It typically takes a couple of body lengths for an instrument to accelerate to the free-fall speed; hence, the upper ~3 m of a profile cannot be used. Surface tracking floats equipped with high-resolution current profilers offer an alternative platform, recently used to obtain vertical profiles of dissipation rate in the upper 0.5 m of the ocean from open waters across the marginal ice zone (MIZ) (Smith & Thomson, 2019; Zippel & Thomson, 2016).

Near-surface measurements of dissipation rate can be used to identify and quantify the contributions of various processes to vertical mixing rates, and to further constrain characterizations of vertical exchange parameters, such as the friction velocity ($u_\star$), and the gas transfer velocity. Using the velocity fluctuations in three orthogonal directions (u', v', w'), the friction velocity, $u_\star = \left(\langle u'w'\rangle^2 + \langle v'w'\rangle^2\right)^{1/4}$, is the characteristic velocity scale in a boundary layer forced by stress and is equivalent to the square root of kinematic Reynolds stress (or of the momentum flux magnitude). The flux of gas across the air-water interface is determined by the gas concentration difference across the interface, and by the transfer velocity which depends on ε (Loose et al., 2014). In partially ice-covered waters, the transfer velocity can be represented using an effective value which is the sum of relative contributions (quantified by the fraction of open water) from a component for the bulk transfer through the sea ice and a component for the transfer in open water (Loose et al., 2014). In the MIZ, Smith and Thomson (2019) propose an effective transfer rate of surface stress that varies by wave height, ice thickness and concentration, and ice-ocean shear depending on the roughness conditions from open waters through the MIZ.

The friction velocity describes the efficiency of the transfer of momentum between sea ice and the ocean through the boundary layer, and may be calculated from velocity covariances (i.e., momentum fluxes) if these are measured at the ice-ocean interface (see e.g., Cole et al., 2014; McPhee, 2008; Peterson et al., 2017). The stress at the surface is approximately constant over a few meters distance from the boundary, allowing measurements at $\mathcal{O}(1)$ m below the ice to be treated as the boundary stress. If the velocity perturbations are not measured, the turbulent stress is often parameterized using a quadratic ice-ocean drag coefficient, $C_d = u_\star^2/U_{\rm rel}^2$, where $U_{\rm rel}$ is the magnitude of velocity difference between the ice and an oceanic reference layer. An estimate can be obtained assuming neutral stratification (no buoyancy effects) and following the logarithmic velocity profile within the boundary layer (e.g., McPhee, 2008). Thus, as few as two distinct velocity observations within the boundary layer are sufficient to estimate $u_\star$ (velocity profile method). If the relative velocity is obtained using observations from outside of the boundary layer, it is necessary to account for Ekman turning on the shear stress, and this can be accomplished using the Rossby similarity relationship (McPhee, 1992). Steele et al. (1989) and Lu et al. (2011) compiled lists of over 30 observation-based estimates of C_d obtained between 1970 and 1997, with values ranging between 0.13×10^{-3} and 47×10^{-3}.

An alternative approach to estimating $u_\star$ uses the dissipation rate profiles resolved in the boundary layer (dissipation rate method) (Dewey & Crawford, 1988). In a simplified, steady-state local budget balance between

TKE production and dissipation, ε in the boundary layer is proportional to the friction velocity and decays with distance, z, from the boundary $\varepsilon(z) = u_\star^3/(\kappa|z|)$, where $\kappa = 0.41$ is the von Karman constant. Such friction velocity, hence surface stress, estimates were made in bottom boundary layers using dissipation profiles from sinking microstructure profilers on the continental shelf (Dewey & Crawford, 1988; Perlin et al., 2005), in deep dense overflows (Price et al., 1993) and in Bering Strait in the Arctic Ocean (Couto et al., 2020).

The characterization of the Arctic air-ice-ocean system is not sufficiently constrained by observations in the upper meters below the sea ice. This leads to large uncertainties in the estimates of the ice-ocean drag coefficient and momentum transfer rates. Furthermore, the vertical profile of dissipation rate typically varies by orders of magnitude in the boundary layer. To better constrain exchanges of gas, momentum, and heat, it is crucial to resolve the vertical structure of turbulence and its variability in response to different buoyancy and wind forcing, under different sea ice conditions. A better understanding of the processes controlling the under-ice boundary layer will help obtaining more accurate estimates of, for example, the net uptake of CO_2 and sea ice variability in the Arctic Ocean. Here we report on vertical profiles of dissipation rate collected using a new type of ascending profiler, which fills this gap by measuring the turbulence structure up to the ice-water interface. Data were collected during the Multidisciplinary drifting Observatory for the Study of the Arctic Climate (MOSAiC) drift experiment in varying sea ice conditions and wind forcing. The technical motivation of this paper is to document the capability and limitations of this profiling method. The scientific motivation is to use the well-resolved dissipation profiles to discuss the near-surface structure of dissipation rates in different regions and ice conditions and estimate ice-ocean drag coefficients representative for the MOSAiC sampling site. This provides fundamental context on ice-ocean coupling for the larger MOSAiC campaign. In the following section, we introduce the instrument, its setup and the geographical and meteorological context of the measurements. In Section 3, we describe the methods used and further detail the dissipation data processing and friction velocity estimates in Appendixes A and B, respectively. Section 4 presents the results in terms of data quality, variability of dissipation rates, friction velocity, and drag coefficients. The discussion contextualizes our findings which are finally summarized in Section 6.

2. Experiment, Instrument, and Sampling Overview

2.1. The MOSAiC Drift

Data were collected as a part of the Arctic Ocean mixing processes and vertical fluxes of energy and matter (AROMA) project, during the MOSAiC drift experiment. The experiment was supported by the research icebreaker *Polarstern* and divided into five legs for crew exchange. Details about the different legs and physical oceanography sampling can be found in Rabe et al. (2022). The track of the experiment including the passive drift stations and transits is shown in Figure 1.

The drift station was established on 4 October 2019 in the Amundsen Basin, and drifted northwards with a moderate speed of ∼0.1 m s^{-1}, along the Lomonosov Ridge. In spring 2020, the drift speed increased and the floe passed the Gakkel Ridge into the Nansen Basin. After an interruption of the drift between 14 May and 19 June 2020, measurements were resumed on the same floe at the northeastern flank of the Yermak Plateau. After crossing the plateau, this first floe broke apart in Fram Strait in July 2020. A new camp was established on 20 August 2020 in the central Arctic, and sampling continued on a second floe close to the North Pole (see Figure 1), which ended on 20 September 2020.

Routine upper ocean profile measurements at the "Central Observatory" formed an important component of the experiment. The Central Observatory comprised multiple sites on the same ice floe with *Polarstern* as the central base, including the "Ocean City" about 300 m away from the ship, where upper ocean profile measurements were made (for more details see Rabe et al., 2022). The floe maps from legs 4 and 5 show the relative locations of instruments relevant to this study and the Ocean City (Figure 2).

2.2. Microstructure Profiler

Dissipation measurements were made using an internally recording Vertical Microstructure Profiler (VMP-250-IR, SN104, VMP hereafter) from Rockland Scientific International (RSI), Canada. The VMP is battery powered and records time series of small scale shear from two orthogonal air-foil shear probes (one measuring $\partial u/\partial z$ the other

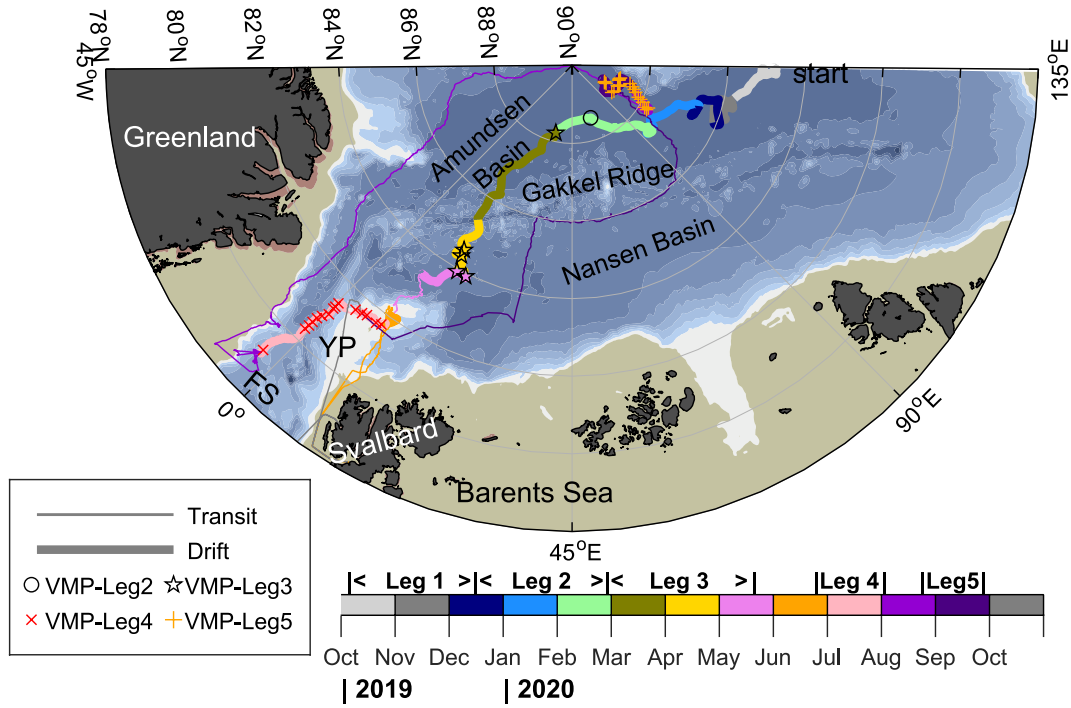

Figure 1. Track of the Multidisciplinary drifting Observatory for the Study of the Arctic Climate (MOSAiC) experiment showing the transit of *Polarstern* (thin) and the passive drift stations (thick line) together with the Vertical Microstructure Profiler (VMP) stations. The positions are shown for each day of profiling conducted in legs 2 to 4 (see legend). Here, the duration of legs is marked only for the drifting floe periods. The MOSAiC track is color-coded in months. YP: Yermak Plateau; FS: Fram Strait.

$\partial v/\partial z$ when profiling vertically), platform vibration using two linear piezo-accelerometers, pressure, and micro-conductivity (SBE7), temperature (FP07), and their gradients at high resolution. In MOSAiC, we configured the instrument to be positively buoyant, an "upriser", by installing a flotation collar close to the front bulkhead of the instrument. Brushes at the tail provided drag to adjust to the desired rise speed. The "upriser" setup and deployment through a hole in drifting sea ice are not standard, hence we provide a brief description here. A sketch of the deployment and profiling procedure is shown in Figure 3.

The internal storage card and a polymer lithium-ion rechargeable battery allow for up to 12 hr of continuous operation. Data acquisition starts by attaching a magnet switch and continues until the magnet is removed. At its tail, the profiler is attached to a light rope and is lowered using a weight-release system (Figure 3a). An approximately 10 kg weight ballast is attached to a mechanical release mechanism connected to an electric cable and a battery-powered deck release controller. The release together with the ballast is attached to a small shackle on the instrument's rope at approximately 3 m behind the tail. This ensures that the ballast can be re-attached to repeat a profile without having to pull the instrument out of water. The instrument is lowered with the attached weight-release system by feeding the rope and the electric cable simultaneously down to 80–100 m depth. The two lines should be separated to the extent practically possible to minimize the risk of entanglement. At target depth, we wait up to 5 min to let the generated turbulence dissipate or advect away. The weight is then released by sending an electric signal to trigger the release mechanism (Figure 3b). As the instrument ascends, the operator waits or slowly recovers the rope to ensure an undisturbed uprising profile. The electric cable with the attached weight is pulled up in parallel. The pulling of the weight ballast generates turbulence. In earlier profiles, this went unnoticed (we removed the contaminated data during post-processing). For the later profiles, to minimize the effect of sampling the wake of the ballast, we wait another minute before starting pulling up the electric cable. An extended probe guard allows hitting the ice without damaging the sensitive shear probes.

A profile continues until the instrument stops at the ice or at the sea surface in leads. As the sea ice moves, the instrument reaches the ice-ocean interface at an unknown distance relative to the deployment position and must be pulled back to the hole or to the edge of sea ice in leads. To avoid dragging the instrument under sea ice, we

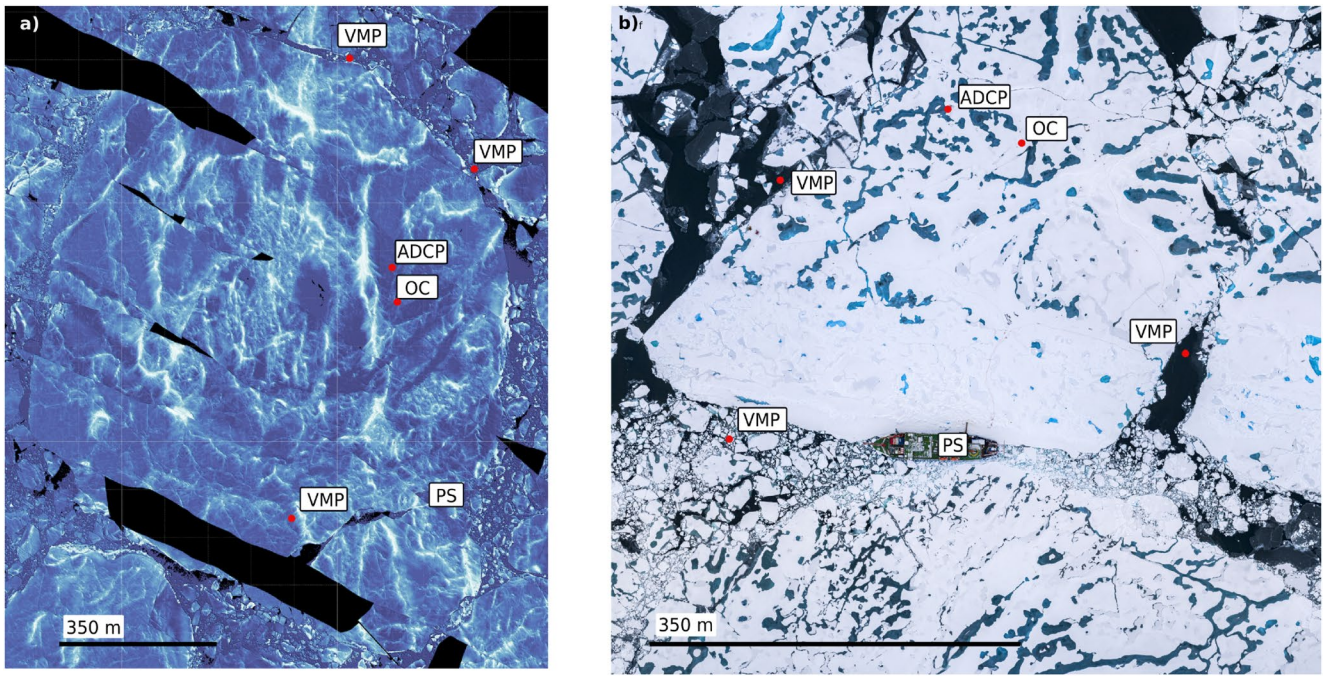

Figure 2. Floe maps from (a) leg 4 and (b) leg 5, showing the profiling locations with Vertical Microstructure Profiler (VMP), relative to *Polarstern* (PS), Ocean City (OC), and the acoustic Doppler current profiler (ADCP). The measurements were taken at OC as well as the locations indicated by VMP. The image from leg 4 is based on preliminary processed data from Airborne Laser Scanning performed on 16 June 2020. Colors indicate surface topography between about 0 (blue) and 1 m (white); regions with missing data are black. Image from leg 5 is obtained from a drone on 6 September 2020 (credit: Alfred-Wegener-Institute/Steffen Graupner, Karl Finkenbeiner).

send a recovery weight along the line to force the instrument down to about 1 m below the ice (Figure 3c). As the line is retrieved, once the shackle above the instrument's tail reaches the operator, the recovery weight is removed, and the weight-release system is re-attached to start a new profile. At the end of the profiling series, the recorded

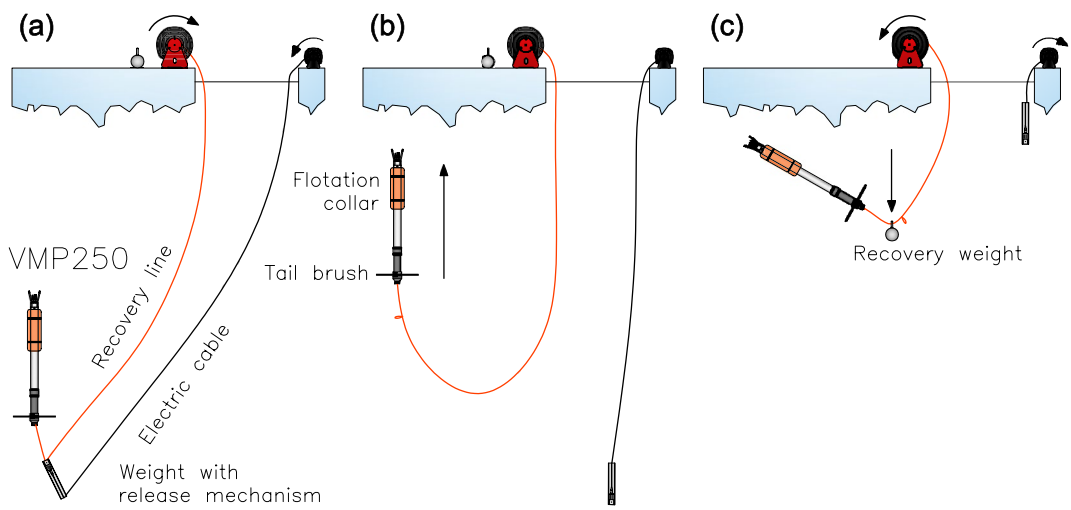

Figure 3. Schematic of the Vertical Microstructure Profiler (VMP) "upriser" profiling procedure through a hole in sea ice. (a) The instrument is attached to a recovery line (red) and lowered into the water using a weight with a release mechanism that is attached to an electric cable (black). (b) The operator triggers the release mechanism and the profiler ascends. (c) The ascent stops when the probe guard of the profiler reaches the ice. The weight with the electric cable and the instrument with the recovery line are hauled back up. A smaller recovery weight is sent sliding down the recovery line to pull the instrument down and thus avoiding dragging it under rough ice during recovery. When the instrument appears again in the hole, the recovery weight is removed and the VMP is prepared for redeployment without removing it from the water.

data are downloaded and the battery recharged. It was practically not possible to obtain profiles when the drift speed exceeded about 0.5 m s^{-1}. For typical drift speeds of 0.1–0.2 m s^{-1}, we expect a negligible lateral drift of about 10–25 m during the profiling time of less than 2 min from 80 m to surface.

2.3. Ocean Current, Wind and Floe Position Measurements

Horizontal ocean current measurements used in this study were obtained using an RD-Instrument Workhorse "Long Ranger" 75 kHz acoustic Doppler current profiler (ADCP), deployed approximately 50 m from the Ocean City. The ADCP pointed downward, rigidly suspended through a hole on the ice floe in each leg of the MOSAiC expedition. During legs 1–3 and 5, the instrument was powered from the ship, and data were logged directly on a personal computer onboard *Polarstern*. During leg 4 the instrument sampled in stand-alone mode. The data together with a detailed report are available from Baumann et al. (2021). The vertical resolution is 8 m and the shallowest depth level for reliable current observations is 22 m.

The floe positions reported here are obtained from a SIMRAD HS60 global positioning system (GPS) receiver that was placed on a mast and deployed on the ice at the same location as the 75 kHz ADCP, hence do not reflect the exact location of the VMP casts. Relative positions of the ADCP/GPS and VMP locations can be seen in Figure 2.

In our analysis, we only use the ice-relative ocean current speed averaged in 20 min intervals (typically 240 profiles every 5 s) but note that the absolute currents in Earth coordinates are available in Baumann et al. (2021). The expected accuracy of the averaged horizontal current measurements is ∼0.01 m s^{-1}.

Wind observations are from measurements at the ship's mast at 39 m height and were extracted at 10 min resolution from *Polarstern*'s continuous meteorological data logging system. The wind observations are not converted to 10 m height, except in the analysis in Section 4.3, where they are clearly identified as W_{10}.

2.4. Stratification and Mixed Layer Depth

The VMP does not have a precision conductivity sensor. Temperature and conductivity records from the VMP were calibrated using the profiles collected from ice or from the ship, closest in time and space. The matching profile was always to within 2 hr of a set of VMP profiles. The fragile microconductivity sensors broke several times during the experiment, because the profiler went through thin sea ice, or the recovery rope got entangled with the probes. No salinity data were available during leg 5 and the last microconductivity measurement was obtained on 28 July 2020. In this study, we do not use the salinity (and therefore density) data from the VMP.

Supplementary high resolution vertical profiles of temperature and salinity are available from a loosely-tethered microstructure profiler (MSS90, Sea and Sun Technology, Germany), collected typically every day at the Ocean City. A detailed description of the data and data processing can be found in Schulz et al. (2022a). We obtain the vertical stratification and the mixed layer depth (MLD) for each day of VMP sampling from all available MSS profiles in that day (typically 5–10, but as many as 55 in intensive sampling days). While the profiling is not co-located in time or space with the VMP (can be up to 500 m distance, see Figure 2), the daily average MLD and stratification will be representative of a VMP day. The stratification is calculated as the buoyancy frequency squared, N^2, using 1 dbar averaged profiles and the International Thermodynamic Equations of Seawater (TEOS-10) (McDougall & Barker, 2011). MLD is estimated as the first depth where density at 5 m depth increased by 0.1 kg m^{-3}. This definition is not particularly tuned for an accurate estimate of a well-mixed layer and may occasionally include 1–5 m thick layer from the pycnocline. The results, however, are representative of the stratification and are not sensitive to small changes in the imposed density threshold. We chose the value at 5 m as the surface value to exclude shallow (1–2 m) melt water layer observed in June and July (Schulz et al., 2022a). Monthly average values calculated over the days with VMP profiling in that month are listed in Table 1.

2.5. Overview of Stations

In total 235 microstructure profiles were collected. Of these, 177 returned data of sufficient quality, 167 profiled to within at least 2 m, and 157 to within at least 1 m of the ice-ocean interface. The number of unique days with data is 37; that is, multiple profiles were obtained in the morning and/or afternoon of a given day. The average

Table 1
Summary of Upriser Microstructure Profiles Performed During the Multidisciplinary Drifting Observatory for the Study of the Arctic Climate Drift

Month	Attempted	Good	Pack ice	Thin ice	Lead	MLD (m)	$(10^5\times)\ N_1^2$ $(\text{rad s}^{-1})^2$	$(10^5\times)\ N_2^2$ $(\text{rad s}^{-1})^2$
February	2	2	2	0	0	41 ± 2	3.7 ± 0.5	49.4 ± 8.7
March	3	3	3	0	0	67 ± 1	2.3 ± 0.3	-
April	11	9	9	0	0	116 ± 4	0.9 ± 0.0	-
May	4	2	2	0	0	138 ± 4	0.7 ± 0.0	-
June	0	0	0	0	0	-	-	-
July	98	66	32	0	34	16 ± 1	22.6 ± 4.8	19.3 ± 1.1
August	41	37	6	11	20	14 ± 1	15.4 ± 3.6	63.2 ± 3.4
September	76	58	14	28	16	17 ± 1	13.0 ± 4.2	87.0 ± 7.2
Total	235	177	68	39	70			

Note. "Good" is the number of profiles with good quality out of attempted profiles. "Pack Ice", "Thin Ice", and "Lead" refer to the ice conditions when the good profiles were collected. Profiles were taken from different locations surrounding the *Polarstern*. The average (± one standard deviation) values of the mixed layer depth (MLD), the stratification between 5 m depth and MLD $\left(N_1^2\right)$, and between MLD and 50 m $\left(N_2^2\right)$ when MLD was shallower than 50 m are also listed.

vertical coverage in the top 10 m was 95%. The majority of data were collected in legs 4 and 5. A summary of the collected profiles is given in Table 1, which also includes the monthly MLD and stratification estimates measured with the MSS at the Ocean City.

The location of the VMP profiling varied depending on the sea ice conditions and logistic constraints. During legs 2 and 3, the VMP was operated from the Ocean City tent on the pack ice. During leg 4, the VMP was operated either from a remotely operated vehicle (ROV) hole on the pack ice (red dot to the left of *Polarstern* in Figure 2a) or from the ice edge into the lead (in the upper right in Figure 2a). Color shading in Figure 2a shows that the ice had significant topography with multiple ridges (white colors) and associated keels. Preliminary results of numerous ice-surveys indicate that the keels reached about 8–10 m depth (Nicolaus et al., 2022, their Figure 9). During leg 5, the VMP was operated from the ice edge in a lead, or from a zodiac or a catamaran more than one ship length in front of *Polarstern* (Figure 2b). The operator categorized the surface conditions of the profile (thin ice/pack ice/open water) depending on the surfacing point of the profiler after its release. Thin ice corresponds to refrozen leads with sea ice thickness less than ∼3 cm. Thicker ice is categorized as pack ice, and open water (lead) when the profiler surfaced.

The average MLD was about 41 m in February, and gradually deepened to 138 m in May. Thus, all our VMP profiles collected in winter and spring are mostly (February) or entirely (March to June) in the mixed layer. During summer, the average MLD was about 15 m (ignoring an occasional shallow, 1–2 m freshwater layer under sea ice). An analysis of pan-Arctic surface mixed layer properties from 1979 to 2012 shows that the eastern Arctic MLDs are typically deeper (20 m in summer, 70 to larger than 100 m in winter), than western Arctic MLDs (8 m in summer, 30 m in winter) (Peralta-Ferriz, & Woodgate, 2015). The observed MLDs during the MOSAiC drift are similar to the long-term average in the eastern Arctic. The average stratification in the mixed layer was 10–20 times larger in July to October compared to that from February to June. The average stratification below the MLD to 50 m depth when the mixed layer was shallower, is also listed (N_2^2 in Table 1). This is representative of the stratification in the pycnocline within the depth range used in this study, and increases about 3 times from July to August and by another 40% to September.

Environmental forcing conditions during VMP casts are summarized in Figure 4. During the first drift (legs 2–3, February–May), all profiles were under pack ice during moderate wind and slow drift conditions. The drift speed over the Yermak Plateau in June was markedly larger, and profiles were collected under solid pack ice. Only after mid-July the ice opened up and allowed for sampling in leads. During the melt season in mid-July, there was a freshwater lens under most of the ice and in the leads (discussed later). Wind speed was moderate to low, but with relatively large drift speeds forced by strong ocean currents. After the final relocation back to the Amundsen Basin in the central Arctic, the variable ice conditions allowed for measurements in pack ice, thin ice, and leads.

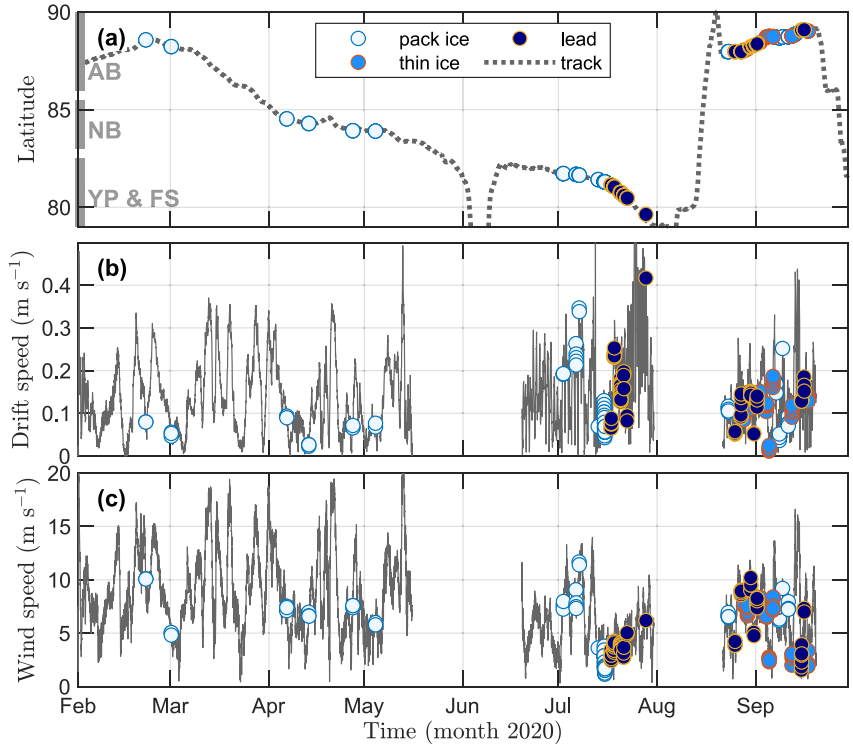

Figure 4. Time series of (a) the latitude of the drift, (b) drift speed, and (c) wind speed at 39 m height. Markers locate the individual Vertical Microstructure Profiler casts, with colors indicating the ice categories. Gray bars in (a) indicate the geographic regions Amundsen Basin (AB), Nansen Basin (NB), Yermak Plateau (YP), and Fram Strait (FS).

Drift speeds in the central Arctic are directly coupled to wind and are generally lower than the strong drift over Yermak Plateau, typically forced by a combination of wind, strong tides and ocean currents.

3. Methods

3.1. Dissipation Rate Estimates

The rate of dissipation is estimated using the isotropic relation (here written for the u component of shear)

$$\varepsilon = \frac{15}{2}\nu\overline{\left(\frac{\partial u}{\partial z}\right)^2} \approx \int_0^{k_c} \Psi(k)\,\mathrm{d}k \tag{1}$$

where ν is the kinematic viscosity, overbar is averaging over time, $\Psi(k)$ is the wavenumber spectrum of shear, and k is the wavenumber in the profiling direction. Another statistically independent estimate is obtained from the second probe measuring $\partial v/\partial z$. Shear probe data processing is detailed in Appendix A.

The ascending part of the time series record from each shear probe was analyzed using 1 s long segments. Dissipation estimates were made over half-overlapping 2 s long records, by integrating the shear spectrum. Particular attention was given to remove portions of the profile affected by the wake of the instrument and the deployment weight. More details on shear spectra calculations, wake contamination, and example spectra are given in Appendix A. The median profiling speed during free ascent was 0.7 m s^{-1} and the noise level of dissipation estimates was below 10^{-9} W kg^{-1}.

Surface impact was identified from the accelerometer data, and was confirmed using records from the microconductivity sensor when available. Vertical distance from sea ice (or free surface) is then obtained for each profile, relative to the measured surface impact pressure. Out of the 157 profiles that returned good dissipation estimates within 1 m of the surface, the average distance to the surface of the first estimate was 0.6 ± 0.1 m (± one standard deviation). The vertical resolution in a dissipation profile was about 0.6–0.7 m, but the dissipation estimates were

independent every 1.2–1.4 m (2 s records). Profiles with respect to the vertical distance from ice (or surface) are obtained by linear interpolation to a uniform vertical grid at 0.4 m resolution for dissipation estimates and 0.1 m for temperature. We do not have reliable salinity and density measurements from the VMP (Section 2.4).

3.2. Friction Velocity Estimates

We obtain the magnitude of friction velocity, u_*, from the dissipation rate profiles resolved in the boundary layer, similar to Dewey and Crawford (1988). When the buoyancy forces are negligible, the dissipation rate, ε, in the boundary layer is proportional to the friction velocity and decays with distance from the boundary, z, $\varepsilon(z) = u_\star^3/(\kappa|z|)$. In practice, however, our method is different from Dewey and Crawford (1988). We determine the values of $u_\star$ using a least-squares fit to ε, similar to Couto et al. (2020).

The method is described in Appendix B, which also shows three example profiles from different regions and ice conditions (Figure B1). Starting with the first three measurement points closest to the surface, we perform nonlinear least-squares fit to $u_\star^3/(\kappa|z|)$ over increasingly more measurement points, and obtain profiles of $u_\star$ and a measure of misfit over increasing depth ranges. For a given profile, the best estimate of $u_\star$ is the one obtained over a depth range with the minimum misfit value. The friction velocity estimates are not sensitive to the number of data points over which the fit is made (Figure B1). A representative boundary layer thickness is analogous to the depth range for which predicted and observed epsilon profiles are in best agreement, as determined by the minimum in the profile of misfit.

4. Results

4.1. Quality of Turbulence Measurements

The instrument profiles up to the ice-water interface or the surface in leads. This allowed us to measure dissipation rates of turbulent kinetic energy in the surface boundary layer or under-ice boundary layer.

The quality of ε estimates can be assessed by comparing the observed shear spectrum to the "Nasmyth" spectrum for the obtained estimate of ε (Appendix A). Although instantaneous spectra can be noisy and deviate from the Nasmyth form, average spectra for similar values of ε are typically represented well by the Nasmyth spectrum. Deviations from this form may indicate contamination of the shear observations (e.g., from instrument movement, instrument vibrations, electronic noise, or particles hitting the probes). It is common practice to remove contamination from the profiler vibration using the piezo-accelerometer data, and applying the so-called Goodman algorithm (Goodman et al., 2006). An accurate application of this method, however, requires multiple segment lengths for cross-spectral calculations to detect coherent shear probe and accelerometer signals. The long segments for spectral analysis coarsen the vertical resolution of dissipation estimates. Because we aim to resolve the dissipation profile close to the sea ice, we do not apply the Goodman algorithm but exclude segments after visual inspection for vibrations or other contamination.

Example profiles from Fram Strait demonstrate that observed spectra in a turbulent layer under ice agree well with each other and do not show distinct narrow-band contamination from vibrations coherent with the accelerometer spectra in the frequency range of interest (Figure A1b). When turbulence levels are lower, observed spectra are closer to the noise level of the instrument, making them more susceptible to vibration contamination. Spectra obtained from a deeper, weakly turbulent layer (Figure A1c) suggest that instrument vibrations dominate shear spectra at frequencies above 10 Hz.

Overall, the data quality from the shear probes on the upriser VMP is good, after excluding segments with a poor figure of merit (Appendix A) and apparent wake and vibration contamination. Shear spectra averaged in bins of ε adhere to the Nasmyth form (Figure A2). Based on the shape of the spectrum and the appearance of vibration contamination, we expect reliable dissipation measurements for values of $\varepsilon > 10^{-9}$ W kg^{-1}.

4.2. Variability of Dissipation Rate in the Upper 50 m

Dissipation profiles regionally categorized into the Amundsen Basin (AB), Nansen Basin (NB), Yermak Plateau (YP) and Fram Strait (FS) cover 4 orders of magnitude from the noise level below 40 m depth to 10^{-5} W kg^{-1} in the surface boundary layer (Figure 5). Generally, the dissipation rate decreases vertically with distance from the

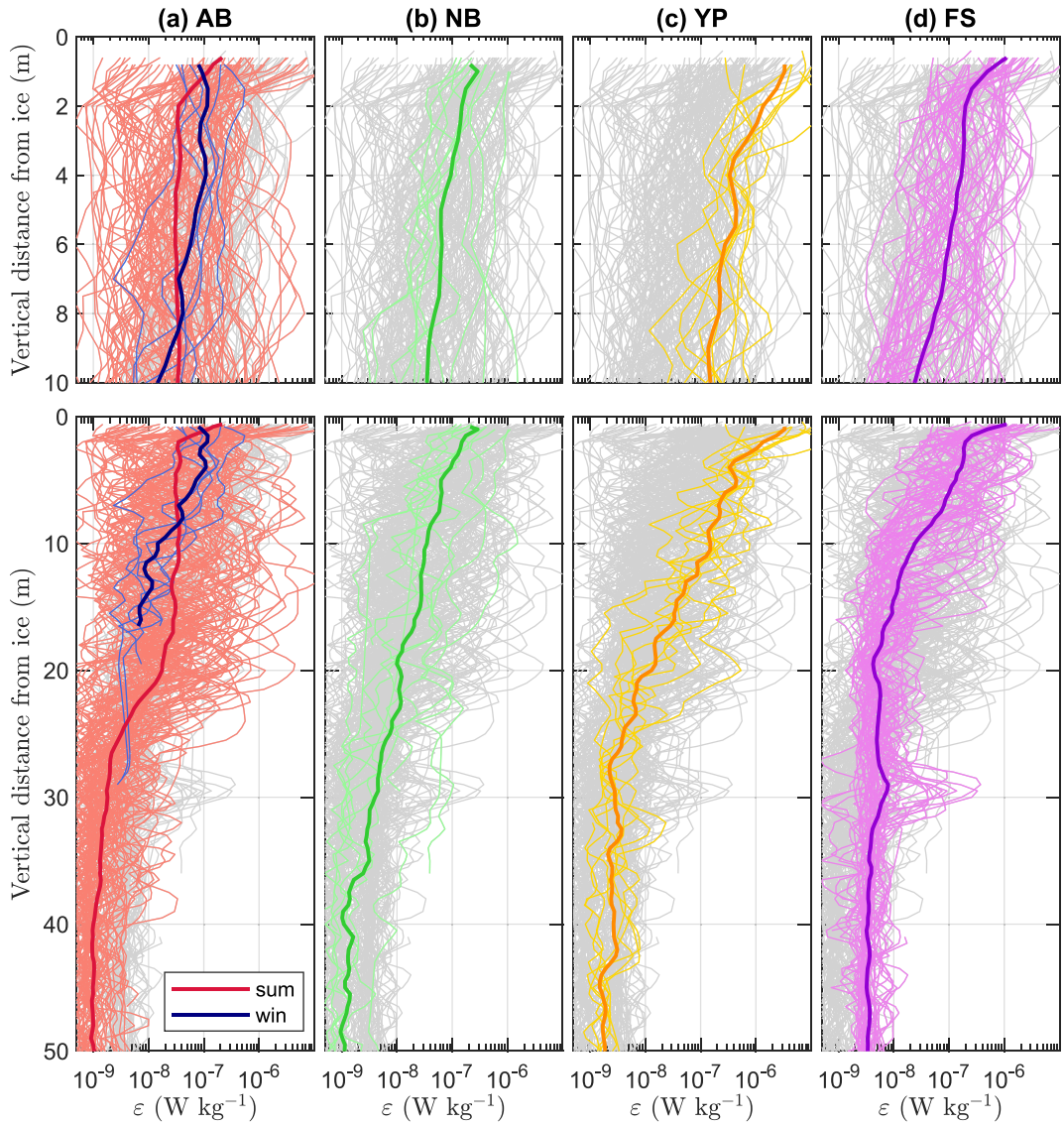

Figure 5. Profiles of dissipation rate, ε, obtained from measurements in (a) Amundsen Basin (AB) in winter (blue) and summer (red), (b) Nansen Basin (NB), (c) Yermak Plateau (YP) and (d) Fram Strait (FS). Each panel shows all good profiles (gray) collected throughout the experiment and the selected subset of profiles highlighted in colors, to allow easy comparison. Vertical distance is measured from the ice-ocean interface or from the sea surface when in open water. Each profile is plotted for both 0–10 m (upper row) and 0–50 m (bottom row). The thick profiles are averages calculated using geometric mean.

ice in the upper 25 m, and increases regionally from the central basins to the Yermak Plateau and Fram Strait. Below 25 m, the average FS profile is above the lowest detection level of the instrument and at least a factor of two more turbulent than the AB and NB profiles.

The mean winter profiles in the AB and NB are quite similar, with moderate turbulence under pack ice, decaying with depth. However, in the NB, there are individual profiles exhibiting greater turbulence, reaching 10^{-6} W kg^{-1} at 10 m under the ice (Figure 5b). The NB profiles were collected in 4 sets. The 3 profiles showing relatively turbulent upper ocean were all from 6 April. The wind speed peaked at 18.5 m s^{-1} in the night of 31 March and remained between 13 and 15 m s^{-1} between 2 and 3 April, suggesting the turbulence was driven by wind-induced processes, such as near-inertial shear.

During the drift over the Yermak Plateau, profiles were typically collected from pack ice (Figures 1 and 4). The drift was dominated by tidal currents (Section 5). In general, the fast drift over YP led to the highest under-ice ε of the whole expedition, averaging $\sim 5 \times 10^{-6}$ W kg^{-1} (Figure 5c).

From the YP to FS, sampling conditions transitioned from pack-ice to leads (Figures 1 and 4). This transition is likely responsible for the broad range of ε under the ice, spanning almost two orders of magnitude. The profiles in FS were collected during moderate to low wind speed; however, the drift speed was highly variable, reaching the maximum magnitude 0.6 m s^{-1} during the experiment. On 20 July, all 12 good profiles collected between noon and 14:30 UTC consistently recorded a 3–4 m thick turbulent patch at about 30 m depth. During the period of measurements, wind was relatively calm with an average speed of 3.7 m s^{-1}, and the drift speed was moderate at 0.15 m s^{-1}. We note that this turbulent patch was also detected in the independent vertical microstructure profiles collected from the Ocean City, and is natural turbulence. FS profiles averaged for pack ice conditions do not show this patch (compare Figures 6a and 6c), implying a link to thin ice or lead conditions. Contrasting the average FS profiles obtained from pack ice with those from thin ice and leads, we also note that ε in the upper 10–15 m is greater under pack ice. While the difference in the vertical structure in the upper 2 m can be related to the strong stratification from the warm freshwater layer observed in the lead profile, the generally elevated levels in the upper 15 m under pack ice could be related to the TKE generation by ridges and keels (Fer & Sundfjord, 2007) (note the ridge near the bottom-most VMP station in Figure 2a).

During summer (August–September), intensive sampling in the AB covered a broad range of under-ice ε in all ice conditions. Although the difference in the number of profiles does not allow a formal comparison, the vertical structure of the mean profiles in the AB differs from winter to summer (compare blue and red profiles in Figure 5). In winter, ε in the upper 8 m under the ice is larger than in summer (except immediately under ice), and subside quickly with depth, to levels less than the summer average. The summer a profile is characterized by large dissipation in the boundary layer followed by near-constant ε down to 20 m, and an abrupt decrease approaching noise level by 25 m under the ice. Categorized with respect to thin ice and leads, summer dissipation profiles in the AB are considerably more energetic in leads (compare solid and dashed red lines in Figure 6c), and the surface warming in leads combined with enhanced turbulence resulted in a warmer upper ocean (Figure 6d).

Figure 7 shows that under pack ice, the dissipation rate in the upper 20 m increases markedly for high drift speeds over 15 cm s^{-1}. Medium drift speeds (7–15 cm s^{-1}) are associated with higher ε in the upper 5 m compared to low drift speeds (<7 cm s^{-1}), but deeper down, the difference is less than a factor of two. Under thin ice and in leads, average profiles of ε show different variability with respect to drift speed. While faster drift is associated with substantially greater dissipation rates immediately below the surface, ε decays quickly with depth and falls below the levels of moderate and slow drift speeds between 10 and 20 m.

A detailed inspection of the thin ice and lead profiles for the slow drift speed subset suggests that this different variability with respect to drift speed should not be generalized. The slow drift set is composed of (a) 3 profiles in FS (dissipation decaying from 10^{-6} W kg^{-1} at 1 m to less than 10^{-8} W kg^{-1} at 10 m), (b) 7 relatively quiescent profiles in the AB, with 10^{-9} to 10^{-8} W kg^{-1} collected on 31 August and 5 September, and (c) 6 exceptionally energetic profiles in the AB collected on 25 August, where dissipation was nearly uniform at about 10^{-6} W kg^{-1} down to 20 m depth. These six profiles dominate the average profile in Figure 7b (green). On 25 August, the wind was weak (2–5 m s^{-1}). Before the set of profiles was taken, the wind vector rotated one full cycle from mid-day 22 August to 24 August while the wind speed was approximately constant between 5 and 8 m s^{-1}. Although not strong forcing, we propose the wind-forced motions of thin ice and inertial shear act to generate the observed levels of turbulence. Energetic dissipation rates modulated by near-inertial waves were previously observed in the AB (Fer, 2014). Excluding the 25 August set would result in a profile with dissipation levels less than the moderate drift speed profile. The relative large surface values for slow drift speeds, both in pack ice and thin ice and leads, are dominated by the YP&FS sets. This region is close to the MIZ, and we can expect a relatively strong contribution of attenuated surface gravity waves that can effectively transfer momentum when the ice-relative velocity is small (Smith & Thomson, 2019). This is discussed later in Section 5.

4.3. Friction Velocity and Drag Coefficient

Time series of $u_\star$ are shown in Figure 8 together with the wind speed, drift speed, and the ice-relative current speed. The friction velocity varied between 1–15 mm s^{-1}, with the largest values in July over the shallow part of

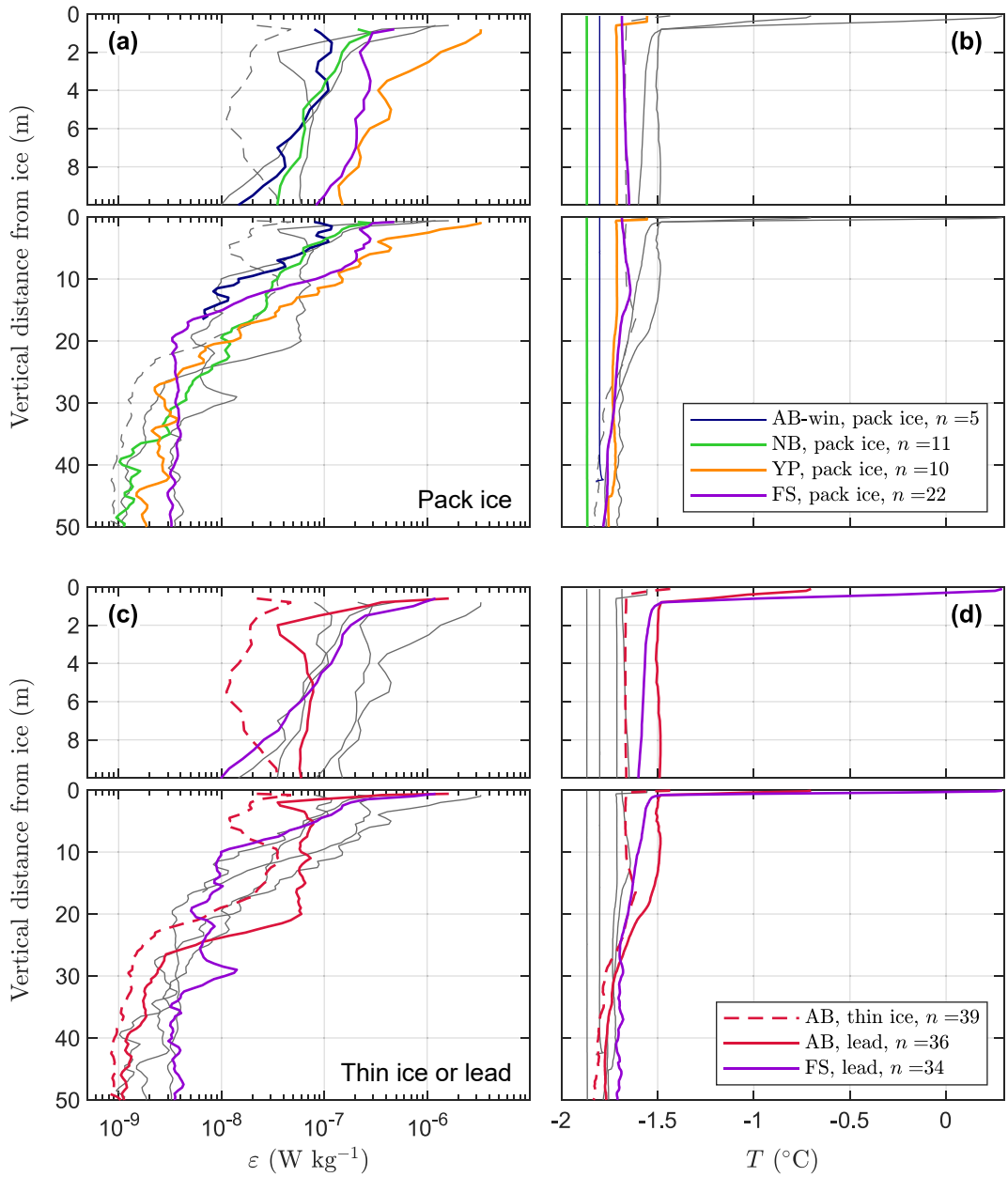

Figure 6. Average profiles of (a and c) dissipation rate (ε, geometric mean) and (b and d) temperature (T) categorized in geographical regions (Amundsen Basin (AB), Nansen Basin (NB), Yermak Plateau (YP), Fram Strait (FS)) and ice type. Vertical distance is measured from the ice-ocean interface or from the sea surface when in open water. Each panel shows all average profiles (gray) collected throughout the experiment and the selected subset of profiles highlighted in colors, to allow easy comparison. Each profile is plotted for both 0–10 m and 0–50 m. The number of profiles, n, included in each category is indicated.

the Yermak Plateau. The representative boundary layer thickness (Appendix B) varied between 2 and 8 m with a mean and standard deviation of 4 ± 2 m. In the later parts of the experiment, sea ice melt resulted in a relatively warm and fresh layer at the surface. While we do not have reliable salinity records for each cast, the temperature profile shows a relatively warm thin layer at the surface, which is associated with a freshwater lens. The average effect on the temperature profiles can be seen in the thin ice and lead profiles in summer AB and FS (Figure 6d). The upper 1–2 m is characterized by warm water 1–2°C above the freezing point, with a strong vertical gradient. Such strong vertical gradients in temperature and salinity would lead to a strong stable stratification that would suppress turbulence–an effect neglected in the simplified TKE-budget equation assumed in the friction velocity

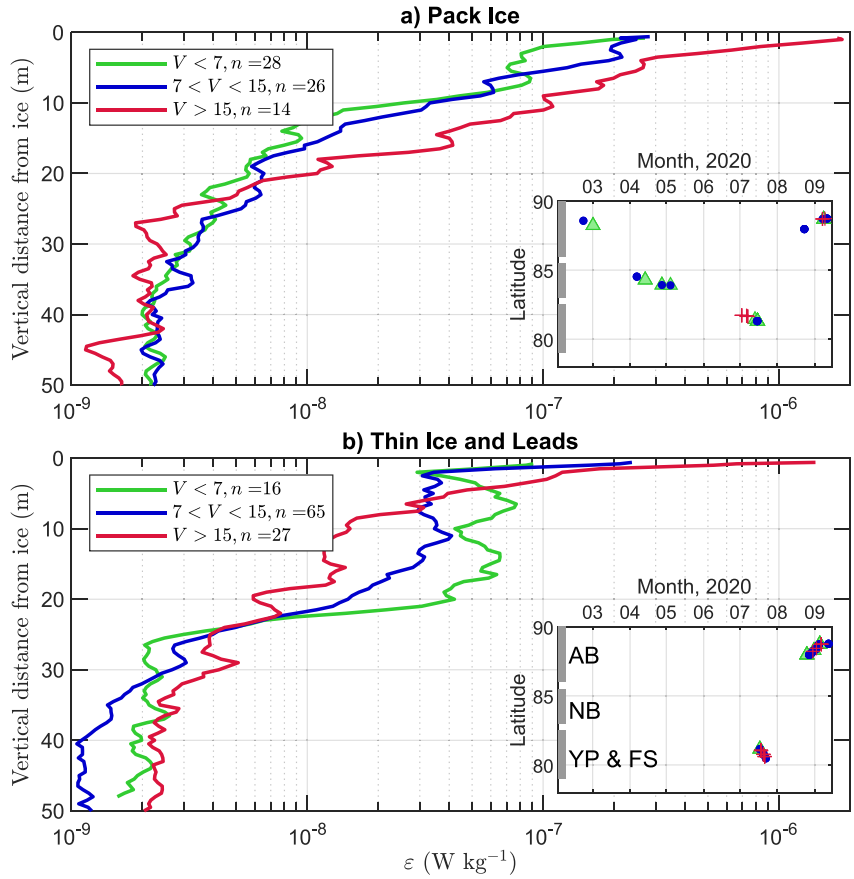

Figure 7. Profiles of dissipation rate, ε, averaged in bins of drift speed (V in cm s^{-1}, see legend) using geometric mean, obtained from measurements in (a) pack ice and (b) thin ice and leads. Vertical distance is measured from the ice-ocean interface or from the sea surface when in open water. The number of profiles, n, included in each bin is indicated. Insets show the time and latitude overview of the profiles with the corresponding colors. Vertical gray bars mark the geographical regions Amundsen Basin (AB), Nansen Basin (NB), Yermak Plateau (YP), Fram Strait (FS).

estimates. We suspect the buoyancy effects to be important in these profiles and expect $u_\star$ estimates to be in error. We identify the profiles with potential buoyancy effect as those with the average vertical temperature gradient in the upper 3 m exceeding 0.5°C m^{-1}. After excluding the data points affected by buoyancy, the average value of $u_\star$ over 132 estimates was 4.7 mm s^{-1}.

The quadratic ice-ocean drag coefficient, $C_d = u_\star^2/U_{\text{rel}}^2$, varies with the magnitude of velocity difference between the ice and an oceanic reference layer, U_{rel}. When the upper surface layer moves together with the sea ice, the relative velocity can vanish even in strong drift speeds (see e.g., Figure 8b: in late July strong tidal currents seen in the drift speed in Fram Strait were absent in the ice-relative current). To obtain the drag coefficient, we use the ice-relative current at 22 m depth from the 20 min time-averaged profiles measured by the ADCP installed on ice. Using the friction velocity obtained for each dissipation profile and the corresponding ice-relative ocean current speed, we estimate C_d. U_{rel} was available in 116 of the 132 $u_\star$ estimates when buoyancy effects were negligible. One estimate is obtained from the regression of u_*^2 against U_{rel}^2, giving a 95% confidence interval of (2–3) $\times 10^{-3}$ (Figure 9a). A second estimate is obtained from the probability distribution function (PDF) of $\log_{10}\left(u_\star^2/U_{\text{rel}}^2\right)$. A maximum likelihood estimator from a lognormal distribution sets the lower and upper limits as (4–6) $\times 10^{-3}$. There is large scatter in the data and the regression method indicates roughly the same C_d value for pack ice, leads, and thin ice, suggesting that this metric represents a broader area of sea ice. The PDF-based estimate, on the other hand, can be affected by the local ice topography and is discussed in Section 5.

During free-drift conditions, when the internal ice stress is not important in the force balance, Arctic pack-ice drift can be approximated as about 2% of the speed of the wind at 10 m height (W_{10}). For the MOSAiC drift, we

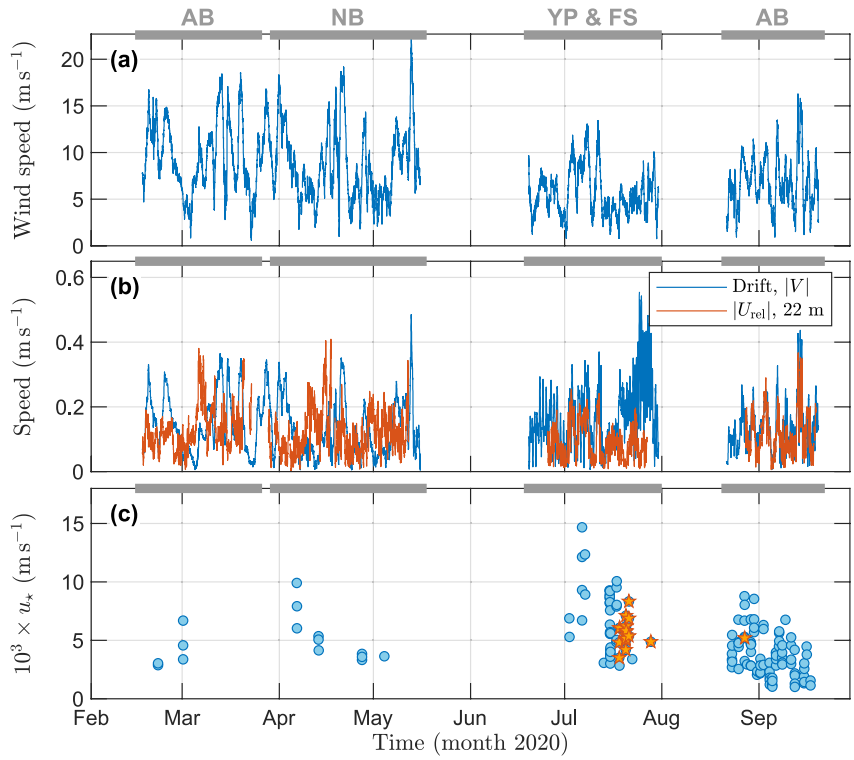

Figure 8. Overview of the friction velocity estimates in relation to wind and drift speed. (a) Hourly-smoothed 10 min wind speed, (b) hourly-smoothed 10 min global positioning system-derived drift speed (blue), and hourly-smoothed 20 min ice-relative ocean current speed measured at 22 m depth (red). (c) Friction velocity from each Vertical Microstructure Profiler profile sampled in the under-ice boundary layer. Orange pentagrams mark the profiles affected by buoyancy fluxes. Gray bars indicate the geographic regions Amundsen Basin (AB), Nansen Basin (NB), Yermak Plateau (YP), and Fram Strait (FS).

calculate the filtered drift velocity using complex demodulation of the drift position time series (Equation 5.11 of McPhee, 2017), removing contributions of rotary diurnal and semidiurnal (also includes the inertial band) frequencies over daily segments, and calculate W_{10} from the measurements at 39 m height using the neutral drag relation in Large and Pond (1981). The average ratio was rather low and varied between 1.6% and 1.8% in the AB, NB, and YP regions (Figure 10). The AB was visited in winter and late summer, but the values of V_0/W_{10} are identical within errorbars, suggesting a lack of seasonal variability in the central Arctic. Diurnal tidal currents, which are typically enhanced over the northern flanks of the Yermak Plateau (Padman et al., 1992), dominated the drift speed over the YP (see the diurnal clockwise rotating component in Figure 10a); however, the drift-wind ratio was close to the free-drift ratio. Fram Strait stands out, where the ratio between ice speed and wind speed averaged to (4.4 ± 1.8)% with a maximum exceeding 10%. Since wind speeds were rather low during this time (Figure 8) and drift velocity was dominated by the semidiurnal component (Figure 10a), it may be expected that semidiurnal tides were responsible for the relatively high drift speed.

5. Discussion

Dissipation profile observations in the Arctic Ocean are scarce in general, and during winter in particular. Furthermore, those that measure to within 1 m of sea ice are rare. While most earlier profiling observations concentrated on the subsurface turbulence, particularly with respect to the turbulent heat flux from the deeper warm layers toward the sea ice, we extract near-surface dissipation values from their published results and compare them to the present study (all dissipation rates below are given in W kg^{-1}). In the Amundsen Basin (AB, April 2007, drifting pack ice, mean drift speed = 0.12 m s^{-1}, MLD = 38 m), ε at 3 m below ice was about 10^{-7}, decaying to 10^{-8} at 25 m (Fer, 2014). During the MOSAiC drift, the April MLD (also in the AB) is 3 times deeper (Table 1), but the dissipation profiles are comparable (see the winter profile in Figure 5a). A deeper mixed layer implies an integrated effect of turbulent mixing, presumably by a deep-reaching contribution from near-inertial wave

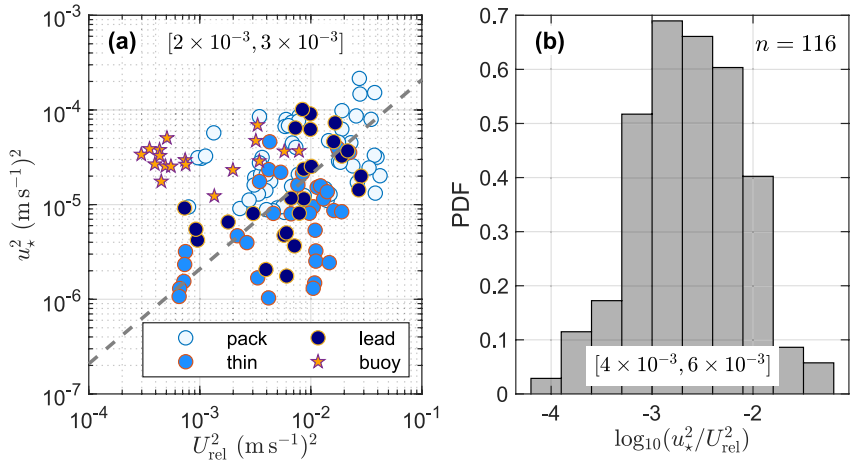

Figure 9. Drag coefficient estimates. (a) Scatter plot of squared ice-relative velocity at 22 m depth, U_{rel} and squared $u_\star$. Data points are color-coded for pack ice, thin ice, and lead profiles. Orange pentagrams mark the profiles affected by buoyancy fluxes. Regression excluding the points affected by buoyancy (with zero intercept, dashed line) gives an estimate of the drag coefficient. 95% confidence interval is indicated. (b) Probability distribution function (PDF) of $u_\star^2/U_{rel}^2$, using a total of 116 data points. Lower and upper bound (95%) estimates from a maximum likelihood estimator from lognormal distribution are indicated.

induced mixing (Fer, 2014). During winter, in the Nansen Basin (NB, February–March 2015, drifting pack ice, drift speed of 0.05–0.15 m s^{-1}, MLD = 60 m), (Fer et al., 2017) report dissipation profiles before and after a storm event. Before the storm, dissipation rates decreased from about 10^{-7} at 2 m to 10^{-8} at 25 m. After the storm, the estimate closest to the surface was above 10^{-6} followed by a quasi-homogeneous ε profile in the upper 20 m with $(5 - 10) \times 10^{-7}$. The 2015 observations before the storm are comparable to the winter profile from the AB and

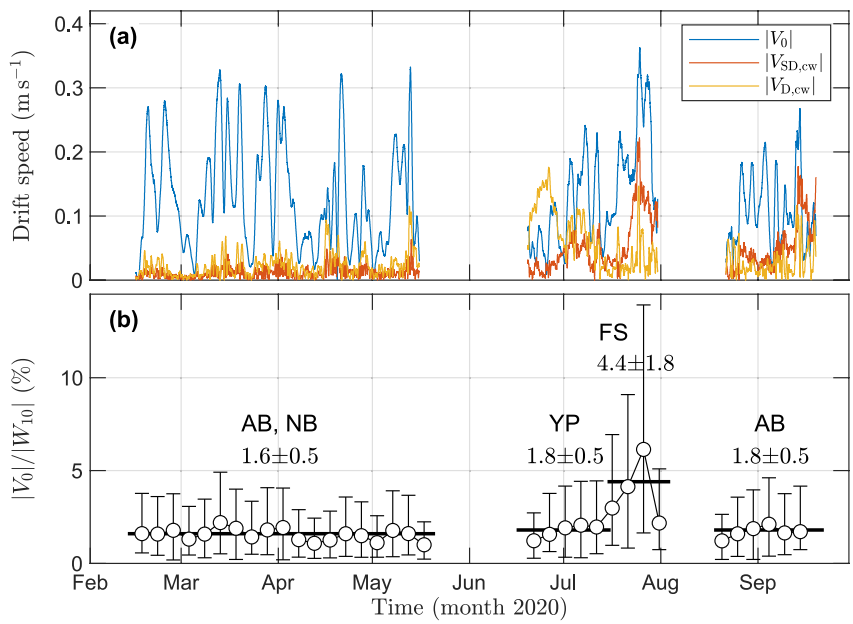

Figure 10. (a) Time series of ice drift speed after complex demodulation using diurnal (D) and semidiurnal (SD, can also be considered inertial) frequencies. The background drift speed (V_0, with D and SD contributions removed) and the clockwise rotating components of V_D and V_{SD} are shown. (b) The ratio (as percentage) of drift speed V_0 to wind speed W_{10} at 10 m height estimated from the measurements at 39 m height using the neutral drag relation in Large and Pond (1981). Markers and error bars are averages and standard deviations over 5 days intervals. The segments in Amundsen Basin (AB), Nansen Basin (NB), Yermak Plateau (YP), Fram Strait (FS) are highlighted with their corresponding average (±1 standard deviation) values.

the profile from the NB (April–May) during MOSAiC. Similar to the profile after the 2015 storm, the set of three profiles (6 April 2020) collected after wind events in the NB are one order of magnitude larger and relatively homogeneous with depth. This implies that typical Arctic storms are expected to generate turbulent mixing layers with ε of $\mathcal{O}\left(10^{-6}\right)$ in the upper 20 m.

In the boundary layer under freezing leads (April 1992, $u_\star = 0.7$ cm s^{-1}, MLD = 30 m), dissipation rates at 10 m varied between $(0.5 - 1) \times 10^{-7}$, and the production was dominated by buoyancy flux from ice freezing (McPhee & Stanton, 1996). All our lead observations are during summer conditions and cannot be compared directly to the convective conditions observed in McPhee and Stanton (1996). We speculate the steep increase in ε in the upper 2 m for leads in AB and FS (Figure 6c) is due to increased momentum input from wind in the exposed open water. Thin ice attenuates this by a factor of two throughout the MLD and by one order of magnitude in the upper 1 m. In other words, we might expect increased energy input from wind to turbulence in the upper ocean in an Arctic with a larger lead fraction.

In the MIZ of the Barents Sea, Fer and Sundfjord (2007) contrasted profiles from open water to 80%–90% ice concentration with ice thickness ranging from 1 to 3 m and keel depths reaching 6 m (spring 2005, MLD of 9–24 m). At the ice-covered stations, ε in the mixed layer varied between 10^{-6} and 10^{-5}. These values are typically larger than our observations, but compare reasonably well with the upper 10 m of the YP pack ice profiles. In the Barents Sea observations, enhanced dissipation averaged over the mixed layer was induced by the pressure-ridge keels. Similarly, we observe increased turbulence in the FS pack ice (characterized by pressure ridges) relative to the lead profile (Figure 6). Although it is not possible to draw firm conclusions from our data set due to a limited number of profiles and averaging over regional and temporal variability, ridge keels can increase the dissipation rate averaged in the upper 10 m by a factor of 4–5 and can be important for the effective momentum transfer of an ice floe.

In another MIZ study form the western Arctic, with focus on the subduction of a warm water jet in the Canada Basin, MacKinnon et al. (2021) reported high-resolution turbulence observations from ship-based microstructure profiling and from Surface Wave Instrument Floats with Tracking (SWIFT) drifters (September 2018, open water, shallow MLD of about 5 m). SWIFT drifters measure ε in the upper 0.5 m. Average dissipation profile linearly increased from 10^{-8} at 20 m to about 10^{-6} at 2 m, and up to about 10^{-4} at 0.5 m. In open waters, dissipation rates can be very large, as a result of breaking surface gravity waves and the short waves acting as roughness elements effectively transferring wind momentum to the upper ocean (Smith & Thomson, 2019; Zippel & Thomson, 2016). The wave amplitudes, and thus the size of roughness elements, are attenuated by sea ice, and accordingly the dissipation rate in the wave-affected boundary layer is reduced (Smith & Thomson, 2019). In the Beaufort and Chukchi Seas MIZ, when ice concentrations were larger than 80% and sea state was low, Smith and Thomson (2019) characterized an "ice-transferred MIZ" regime (the roughness of the surface is set primarily by the ice, rather than the waves), whereby the relative ice-ocean velocity controls the momentum transfer from wind. In such conditions (fall 2015, thin, newly formed ice, SWIFT drifters), the typical ε was $\mathcal{O}\left(10^{-5}\right)$ in the upper 0.5 m (Smith & Thomson, 2019). While we do not have supporting measurements on the penetration of surface waves and swell into the MOSAiC site, the YP sampling location is close to the MIZ and the steep increase of dissipation in the YP in the upper 2 m (Figure 6a) could be related to contribution from swell.

Assuming that the friction velocity estimates from the dissipation profiles are representative of the stress at the ice/ocean interface, the drag coefficient calculated from our data set can be used to obtain the stress from the ice-relative current speed. As discussed in McPhee (2002) in detail, the approach using a constant C_d is valid only in the boundary layer where the velocity profile is logarithmic and the mixing length is $\kappa|z|$. While the friction velocity estimates are from the boundary layer, the ice-relative current used in C_d estimates is from 22 m depth, a considerable distance away from the boundary layer. The vertical distance from ice where the dissipation rate profile could be described by $u_\star^3/(\kappa|z|)$ was 4 ± 2 m (Section 3.2). Beneath the boundary layer, the mixing length is constrained by the Coriolis parameter. The drag coefficient is no longer constant, but depends on friction velocity. The "Rossby similarity" approach (McPhee, 2002, 2017) can be used to obtain an effective drag coefficient. With the data at hand, we cannot apply the method because we lack independent roughness length estimates of the ice flow, and the formulation is dependent on two empirical coefficients, each bearing uncertainties. In Rossby similarity, the surface appears smoother with increasing stress so that the effective drag coefficient decreases with an increased ice-ocean velocity difference (McPhee, 2017). As a result, while the quadratic drag formulation represents the momentum transferred to the ocean well, it is an overestimate for representing the

actual roughness of the ice. Using typical values for roughness length for the Arctic pack ice and the Rossby similarity coefficients, this overestimate can reach about a factor of two for drift velocities of 0.5 m s^{-1} (e.g., see Figure 5.7a of McPhee, 2017). Using continuous observations in the Canada Basin from March through December 2014, Cole et al. (2017) showed that the quadratic drag formulation worked well, except during September in low ice concentration conditions (10%–30%) with small floe sizes.

There is large scatter in the U_{rel}^2 and $u_\star^2$ data points, but there is no systematic difference in their relation for different ice types (differences in slopes are not significant as a result of large scatter and few data points, Figure 9a). The time variability of C_d (not shown) for the individual data points of Figure 9a does not show a clear pattern. The largest values (30–40) $\times 10^{-3}$ were obtained for the 4 profiles collected on 15 July from the ROV hole (the bottom-most station in Figure 2a). These estimates form the right-tail of the distribution in Figure 9b. Similar to other field observations, we speculate that the variations can be attributed to differences in under-ice topography and the direction of the flow relative to the ice keels in the vicinity (cf., Nicolaus et al., 2022). Using our limited data set, we cannot delineate the source of variability in C_d. Because our observations are collected from different ice conditions at varying distance to under-ice roughness elements, we propose that the 95% bounds of (4–6) $\times 10^{-3}$ from the maximum likelihood estimator from lognormal distribution would be representative of the MOSAiC ice floe.

Our drag coefficient and friction velocity estimates can be compared to other observations. A summary table is compiled in Lu et al. (2011) for several field investigations, covering from smooth ((1–8) $\times 10^{-3}$) to rough ((20–22) $\times 10^{-3}$) floes. Using observations from an ice-tethered profiler equipped with a velocity sensor during a 6-month drift in winter 2009–2010 in Canada Basin, Cole et al. (2014) obtained a median value of $C_d = 10 \times 10^{-3}$. In the same region from March through December 2014, median values from 4 different drifting platforms varied between 1×10^{-3} and 4×10^{-3} (Cole et al., 2017). For the Surface Heat Budget of the Arctic Ocean (SHEBA) drift, McPhee (2002) obtained monthly average values varying between 2×10^{-3} and 8×10^{-3}, with a seasonal variability showing the largest values in September–November and the smallest in April–July. In our data set, the friction velocity varied between 1 and 15 mm s^{-1} with an average value of 4.7 mm s^{-1}. From autonomous, ice-based observing systems repeatedly deployed in the Transpolar Drift of the Central Arctic from 2002 through 2010, the average values for each year varied between 6 and 9 mm s^{-1}, with an ensemble average of 7.8 mm s^{-1} (Stanton et al., 2012). Overall, these comparisons suggest that the MOSAiC site is representative of the Arctic sea ice in 2000s.

For the MOSAiC drift, the average ratio between the background ice-drift speed and wind speed V_0/W_{10} was 1.6%–1.8%, close to the free-drift condition, and with no apparent seasonal variability in the central Arctic (Figure 10). Similarly, during the winter drift (2009–2010) in Canada Basin, Cole et al. (2014) obtained an average ratio of 1.9%. The lack of seasonality and close to free drift conditions in winter seen in the observations from last decades imply less resistance from internal ice stress gradients, and relatively thin and/or loose sea ice. For comparison, McPhee (2002) reported a substantial seasonal signal during the Arctic Ice Dynamics Joint Experiment (AIDJEX, 1975), when the winter ratios were about 0.5%. During the SHEBA drift (1997–1998), the seasonal variability was less pronounced but discernible (McPhee, 2002). In both drifts, the summer values were close to 2%, similar to ours and other estimates in 2000s, but now observed throughout the year in the central Arctic.

The vertical structure of turbulence observations and the estimates of surface friction velocity and the neutral drag coefficients were made possible using a setup allowing ascending profiling measurements up to the surface. The use of this system with two lines (one recovery rope and one electric cable) is challenging, particularly when deployed through a hole in ice. Of the attempted profiles, 25% were completely discarded because of various issues disturbing the free ascent or breaking probes. Of the remaining profiles, substantial segments of data were flagged bad, typically contaminated by the wake of the profiler or the release weight. The effort put in collecting the profiles as well as post-processing the data is considerable, and must be weighted against other systems offering continuous point measurements or limited profiling capability using high-resolution current meters or profilers.

6. Summary

A microstructure profiler used in ascending configuration resolved the turbulent kinetic energy dissipation rates ε in the boundary layer under drifting sea ice and in open water leads during the MOSAiC drift. In total, shear probe records from 167 profiles are analyzed, covering from February to mid-September 2020, and spatially from 89°N to 79°30′N through the Amundsen Basin, Nansen Basin, Yermak Plateau, and Fram Strait. Structure and magnitude of the dissipation profile in the upper 50 m varied over time and space, by over 4 orders of magnitude from 10^{-9} W kg^{-1} below 40 m depth to above 10^{-5} W kg^{-1} at 1 m below sea ice. The range of mean dissipation rate at 1 m below ice was 10^{-7}–10^{-6} W kg^{-1} and decreased to 10^{-9}–5×10^{-8} W kg^{-1} near the base of the mixed layer. The largest under-ice ε values were observed over the tidally active Yermak Plateau. Under pack ice, ε subsided rapidly with vertical distance from ice; however, following wind events, energetic turbulent mixing layers with ε of $\mathcal{O}\left(10^{-6}\right)$ extended down to 20 m depth. In exposed open waters of leads in the central Arctic, we observed one order of magnitude increase in ε in the upper 2 m, and about a factor of two increase throughout the mixed layer, relative to thin ice conditions. Profiles near pressure ridges suggest that ridge keels can increase the dissipation rate averaged in the upper 10 m by a factor of 4–5 and can be important for the effective momentum transfer of an ice floe.

The unique under-ice profiles of ε from the upriser allow us to estimate surface friction velocity under ice. Together with the ice-relative ocean current measurements, we obtain ocean-ice drag coefficients over a large range of Arctic conditions. The friction velocity varied between 1 and 15 mm s^{-1} with an average value of 4.7 mm s^{-1}. The boundary layer thickness was estimated to 4 ± 2 m. A representative range of drag coefficient for the MOSAiC sampling site was estimated to $(4–6) \times 10^{-3}$, which the canonical value for Arctic floe observations. Estimates of the ratio of drift speed to wind speed are on average close to the free-drift ratio of 2% with no clear seasonal or regional variability. A notable exception is Fram Strait, where sea-ice drift was likely dominated by strong semidiurnal tidal currents.

Using a microstructure profiler in ascending configuration is relatively complex–both in operation and processing–compared to a standard free-falling set-up, but allows collecting profiles of dissipation rate in the immediate under-ice boundary layer. Despite the shortcomings of the profiling system, we find the data quality from the shear probes on the upriser profiler to be good and suitable for upper-ocean applications in Arctic conditions. Future similar datasets can help advancing the understanding of ice–ocean interactions and their parameterizations in numerical models.

Appendix A: Shear Probe Data Processing and Shear Spectra Overview

In our notation and processing of the shear probe data, we follow the recommendations and conventions of the SCOR Working Group on analyzing ocean turbulence observations to quantify mixing (ATOMIX, http://wiki.uib.no/atomix).

We analyze the time series records as the VMP ascends, after it is released at its target depth. The ice or sea surface was identified from the accelerometer data, and was confirmed using records from the microconductivity sensor when available (the primary microconductivity sensor broke on 13 July, and the spare sensor on 28 July). The pressure record was referenced to the corresponding surface, giving the vertical distance from ice for each profile.

The sampling frequency of the VMP was 512 Hz for turbulence probes and 64 Hz for the slow channels. The ascending part of the time series record from each shear probe was analyzed using 1 s fast Fourier transform (fft) length segments. Dissipation estimates were made over half overlapping 2 s long portions, that is, using average spectrum over 3 segments. Each segment was despiked, detrended, and smoothed using a Hanning window before calculating the spectrum. Vertical speed was obtained from the rate of change of smoothed, high-resolution pressure record, and used to convert frequency domain to vertical wavenumber domain. Shear probe wavenumber spectra were corrected for the probe's spatial response following Macoun and Lueck (2004).

The shear variance is obtained by integrating the spectrum to an upper wavenumber limit, k_c (Section 3). The integration limit is estimated as the wavenumber of the minimum (before the noise takes over) to a high-order polynomial fit to the wavenumber spectrum on log-log space, and was always less than 130 cpm. The correction for the spatial response of a shear probe reaches an order of magnitude beyond this wavenumber, and hence is

avoided. To account for the variance in the unresolved part of the spectrum, that is, outside the integration limits, we used the empirical model for turbulence spectrum determined by Nasmyth (1970), and expressed in the form in (Lueck, 2015), based on the Nasmyth points listed by Oakey (1982).

Goodman coherent-noise reduction algorithm (Goodman et al., 2006) was not applied to ensure sufficient vertical resolution in the boundary layer. The method for noise removal relies on the squared-coherency spectrum between the shear probe signal and the accelerometer signals and its statistical significance increases with increasing number of fft-segments used to make a spectral estimate. Increasing the dissipation estimate length from 2 to 5 s would considerably degrade the dissipation profile resolution, particularly in the boundary layer where dissipation changes strongly with depth.

The figure of merit, FoM = MAD × DOF$^{1/2}$, combines the mean absolute deviation (MAD) and the degrees of freedom (DOF) into one misfit estimate, relative to the empirical Nasmyth spectrum (see http://wiki.uib.no/atomix for details; note, however, that the ATOMIX definitions and recommendations for FoM and the model spectrum were updated and may differ relative to that applied at the time of this analysis). While a threshold for rejection has not yet been devised, FoM is a useful quality-control metric. Values of FoM much larger than one indicate a poor spectral fit, whereas values smaller than one indicate good fits of the measured spectrum to the model spectrum. After inspecting spectra averaged in bins of FoM, we find spectra with FoM ≥2 deviate substantially from the Nasmyth shape, and exclude them from the analysis.

Of the 235 profiles made, 177 were of sufficient quality and yielded a total of 7,676 individual estimates of dissipation rate. When of sufficient quality, estimates from both probes were averaged to obtain the final dissipation rate, as long as they agreed within a factor of five; otherwise, the minimum of the two was used. The typical reason for deteriorated data quality was a broken shear probe after contact with ice, rope or recovery weight, or temporary bad data and spikes from contact with plankton and other particulates in the water. Values from both probes were averaged for 2,436 (32%) of all estimates. For the remaining, estimates relied on only one probe, with

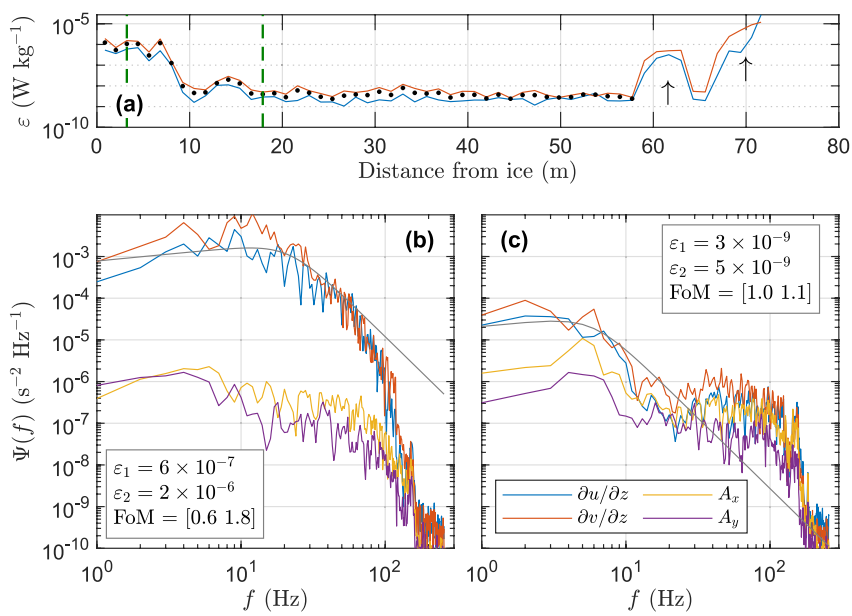

Figure A1. Example spectra from a profile collected on 15 July 2020 in Fram Strait. (a) Dissipation rate estimates from two orthogonal shear probes (blue, $\partial u/\partial z$ and red, $\partial v/\partial z$), and their average (dots) in the accepted portion of the profile. The effects of wake of the profiler (around 70 m) and the wake of the recovery weight (around 60 m) are marked by arrows. Frequency spectra of shear and vibration (from piezo-acceleration sensors) from a 2 s segment in (b) energetic turbulence and (c) relatively quiescent turbulence. The depth of the segments is marked in (a), at approximately 3 and 18 m, respectively. Gray curves are the Nasmyth spectra for the average dissipation rate for each segment. Figure of merit (FoM) is indicated for each shear probe.

a total of 3,911 (51%) estimates coming from probe 1 and 1,329 (17%) from probe 2. When estimates from both probes were available, their individual values for the dissipation rate agreed on average with a factor of 2.1. The FoM was below 1 for 80% and 72% of the estimates for probes 1 and 2, respectively.

Example spectra from 2 s segments (giving a single estimate of ε) are shown from a profile collected on 15 July 2020 in Fram Strait (Figure A1). This profile is chosen arbitrarily, but with a condition to include acceptable data from both probes. The profile also demonstrates the contamination from the wake of the profiler (around 70 m distance from ice) and the wake of the recovery weight (around 60 m). Such segments are excluded from the final average profile by manual screening of the profiles. Dissipation rate estimates from two orthogonal shear components ($\partial u/\partial z$ and $\partial v/\partial z$) agree within an approximate factor of two. There is general agreement with the form of the Nasmyth's empirical spectrum. For the final analyses only estimates with FoM less than 2 are used. Not using the coherent-noise reduction algorithm may lead to relatively large dissipation rate estimates. An example can be seen in the quiescent spectrum for the $\partial v/\partial z$ component, which shows a correlated peak with the accelerometer spectra at approximately 5 Hz. Although the resulting estimate is slightly larger than that from $\partial u/\partial z$, the agreement is within a factor of two.

Next, we show the frequency and wavenumber shear spectra averaged over individual spectra of dissipation values sorted in bins of ε (Figure A2). Nasmyth spectra are shown for the geometric mean of the dissipation rate estimates in each bin (curves for the arithmetic average are similar). Ascent speed is averaged over the values in each bin and is used to convert between frequency and wavenumber domain. Overall agreement with the Nasmyth form is good and implies measurements from the upriser system are of good quality. The noise level, inferred from the deteriorating form of the lowest dissipation bin, is better than 1×10^{-9} W kg^{-1}. Some smearing out of the average wavenumber spectra relative to the Nasmyth form is expected because (a) we average spectra with dissipation values covering one order of magnitude and (b) the vertical speed variability is 10%–20%.

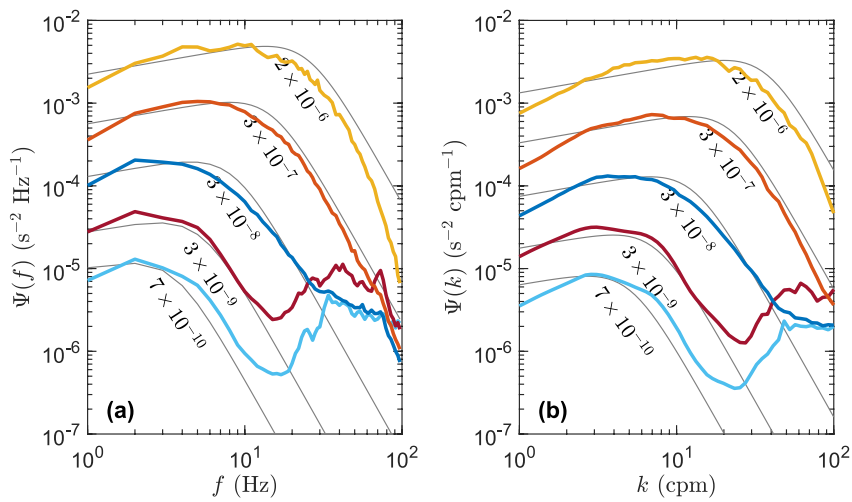

Figure A2. Shear spectra averaged in bins of ε at one decade intervals starting from 1×10^{-10} W kg^{-1} presented as (a) frequency, f, and (b) vertical wavenumber, k, spectra. The number of spectra averaged are, from the lowest bin to the highest, 472; 2,712; 1,151; 708; and 127. Nasmyth curves corresponding to the geometric mean dissipation rate in each bin are shown with the values of ε indicated.

Appendix B: Friction Velocity and Boundary Layer Thickness Estimation

We estimate the friction velocity and a representative boundary layer thickness from the dissipation rate profiles resolved in the upper 2–15 m. Starting from the first three measurement points closest to the surface, we fit each dissipation profile using nonlinear least-squares regression to $u_\star^3/(\kappa|z|)$, and obtain a value for $u_\star$. Via the same relation, this leads in turn to a "predicted" profile of epsilon and a misfit measure over the same depth range. The misfit is calculated as the median value of the ratio of predicted to observed values of dissipation rate (or the inverse ratio if less than one) within the fitted data points. A misfit value equal to 1 is thus a perfect fit. We repeat the procedure for increasingly more measurement points to obtain profiles of $u_\star$ and misfit over increasing depth ranges. For a given profile, the best estimate of $u_\star$ is then the one obtained over a depth range with the minimum misfit value. We use only the profiles (167 in total) with data to within 2 m of the surface and use the dissipation rates in the first 15 m from the surface to exclude eventual subsurface patches of turbulence.

A representative boundary layer thickness is analogous to the depth range for which predicted and observed epsilon profiles are in best agreement, as determined by the minimum in the profile of misfit. When the misfit is larger than 2, we exclude the profile on the grounds that the profile is not well represented by the $1/|z|$ profile, likely a result of ridge keels which can inject turbulence at a larger vertical distance relative to the smooth ice (Fer & Sundfjord, 2007).

The method is shown in Figure B1 for three selected examples with different regions, ice conditions and friction velocity magnitudes: from the Nansen Basin in pack ice, from a lead in Fram Strait, and from thin ice in the Amundsen Basin.

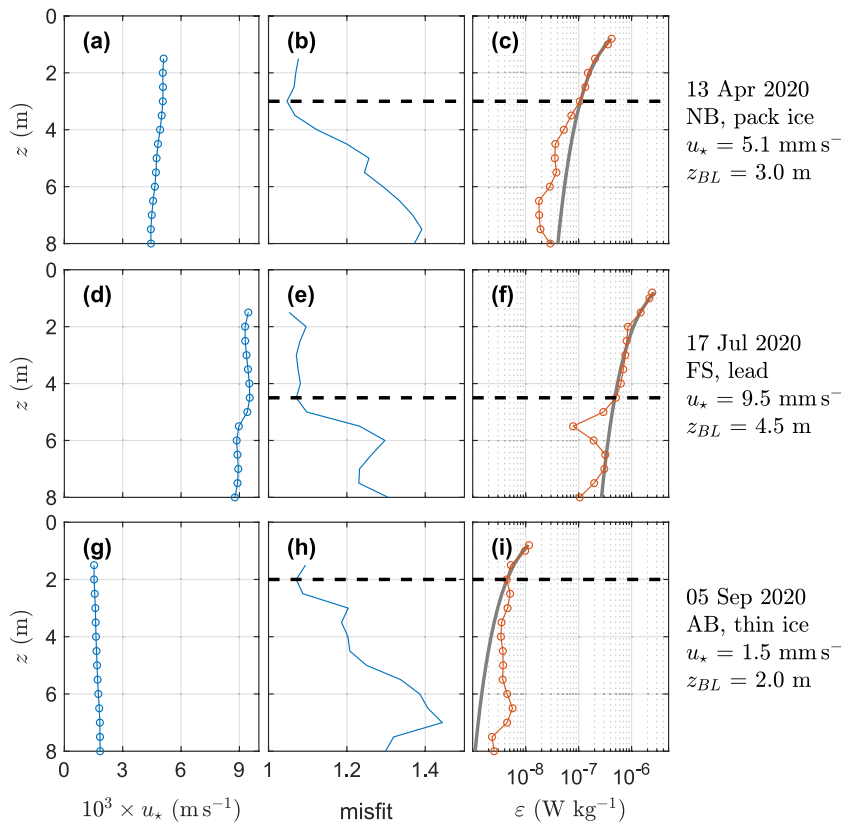

Figure B1. Vertical profiles showing the details of friction velocity and boundary layer thickness estimates for three selected examples. Details are listed on the rightmost column of each row. (a, d and g) friction velocity estimates with increasing number of data points used in the fit (b, e and h) misfit together with the selected minimum (dashed line) identifying the boundary layer depth, z_{BL} (c, f and i) measured dissipation rate profile (red) together with the $u_\star^3/(\kappa|z|)$ (gray) using the best estimate of $u_\star$.

Data Availability Statement

The VMP microstructure data are available from Fer et al. (2022) at https://doi.pangaea.de/10.1594/PANGAEA.946076. The ocean current (ADCP) and floe position (GPS) data are available from Baumann et al. (2021) at https://doi.pangaea.de/10.1594/PANGAEA.934792. The MSS profiler data are available from Schulz et al. (2022b) at https://doi.org/10.1594/PANGAEA.939816. Wind speed measurements from the ship's mast are available under https://dship.awi.de, and a 3 hourly subset of the data was published on PANGAEA at https://doi.org/10.1594/PANGAEA.935264, https://doi.org/10.1594/PANGAEA.935265, https://doi.org/10.1594/PANGAEA.935266, and https://doi.org/10.1594/PANGAEA.935267, for legs 2–5, respectively.

Acknowledgments
The study was funded through the AROMA (Arctic Ocean mixing processes and vertical fluxes of energy and matter) project by the Research Council of Norway, Grant No. 294396. We acknowledge the support of the international Multidisciplinary drifting Observatory for the Study of the Arctic Climate (MOSAiC) project with the tag MOSAiC20192020 and the Project_ID: AWI_PS122_00. We thank the captains and crew of *Polarstern* and the participants who supported the on-site experiments. A detailed acknowledgment for the expedition can be found in Nixdorf et al. (2021). Specifically, we thank Helge Bryhni and Algot Peterson for planning, design, and preparation of the instruments, and fieldwork participants Mario Hoppmann, Ying-Chih Fang, Salar Karam, Ivan Kuznetsov, Kirstin Schulz, Janin Schaffer, Ingo Schuffenhauer, and Natalia Sukhikh for their efforts with data collection in harsh Arctic conditions. The Airborne Laser Scanning image was provided by Luisa von Albedyll, Gerit Birnbaum and Stefan Hendricks. Algot Peterson prepared the drawing of the VMP deployment procedure. MM was supported by the Research Council of Norway, Grant No. 280292. Comments from two anonymous reviewers and Xi Liang helped improve a previous version of the manuscript.

References

Baumann, T., Fer, I., Bryhni, H., Peterson, A. K., Allerholt, J., Fang, Y.-C., et al. (2021). Under-ice current measurements during MOSAiC from a 75 kHz acoustic Doppler profiler [dataset]. PANGAEA. Retrieved from https://doi.org/10.1594/PANGAEA.934792

Carmack, E., Polyakov, I., Padman, L., Fer, I., Hunke, E., Hutchings, J., & Winsor, P. (2015). Towards quantifying the increasing role of oceanic heat in sea ice loss in the new Arctic. *Bulletin America Meteorology Social*, *96*(12), 2079–2105. https://doi.org/10.1175/BAMS-D-13-00177.1

Cole, S. T., Timmermans, M.-L., Toole, J. M., Krishfield, R. A., & Thwaites, F. T. (2014). Ekman Veering, internal waves, and turbulence observed under Arctic sea ice. *Journal of Physical Oceanography*, *44*(5), 1306–1328. https://doi.org/10.1175/JPO-D-12-0191.1

Cole, S. T., Toole, J. M., Lele, R., Timmermans, M.-L., Gallaher, S. G., Stanton, T. P., et al. (2017). Ice and ocean velocity in the Arctic marginal ice zone: Ice roughness and momentum transfer. *Elementa: Science of the Anthropocene*, *5*, 55. https://doi.org/10.1525/elementa.241

Couto, N., Alford, M. H., MacKinnon, J., & Mickett, J. B. (2020). Mixing rates and bottom drag in Bering Strait. *Journal of Physical Oceanography*, *50*(3), 809–825. https://doi.org/10.1175/jpo-d-19-0154.1

Dewey, R. K., & Crawford, W. R. (1988). Bottom stress estimates from vertical dissipation rate profiles on the continental shelf. *Journal of Physical Oceanography*, *18*(8), 1167–1177. https://doi.org/10.1175/1520-0485(1988)018<1167:bsefvd>2.0.co;2

Fer, I. (2014). Near-inertial mixing in the central Arctic Ocean. *Journal of Physical Oceanography*, *44*(8), 2031–2049. https://doi.org/10.1175/JPO-D-13-0133.1

Fer, I., Baumann, T., Fang, Y.-C., Hoppmann, M., Karam, S., Koenig, Z., et al. (2022). Under-ice temperature and dissipation rate profiles from uprising VMP250 during MOSAiC [dataset]. PANGAEA, Retrieved from https://doi.pangaea.de/10.1594/PANGAEA.946076

Fer, I., Peterson, A. K., Randelhoff, A., & Meyer, A. (2017). One-dimensional evolution of the upper water column in the Atlantic sector of the Arctic Ocean in winter. *Journal of Geophysical Research: Oceans*, *122*(3), 1665–1682. https://doi.org/10.1002/2016JC012431

Fer, I., & Sundfjord, A. (2007). Observations of upper ocean boundary layer dynamics in the marginal ice zone. *Journal of Geophysical Research*, *112*(C4), C04012. https://doi.org/10.1029/2005JC003428

Goodman, L., Levine, E. R., & Lueck, R. G. (2006). On measuring the terms of the turbulent kinetic energy budget from an AUV. *Journal of Atmospheric and Oceanic Technology*, *23*(7), 977–990. https://doi.org/10.1175/jtech1889.1

Large, W. G., & Pond, S. (1981). Open ocean momentum flux measurements in moderate to strong winds. *Journal of Physical Oceanography*, *11*(3), 324–336. https://doi.org/10.1175/1520-0485(1981)011⟨0324:Oomfmi⟩2.0.Co;2

Lenn, Y.-D., Fer, I., Timmermans, M.-L., & MacKinnon, J. A. (2021). Mixing in the Arctic Ocean. In M. Meredith & A. C. Naveira Garabato (Eds.), *Ocean mixing: Drivers, mechanisms and impacts* (pp. 275–299). Elsevier. https://doi.org/10.1016/B978-0-12-821512-8.00018-9

Loose, B., McGillis, W. R., Perovich, D., Zappa, C. J., & Schlosser, P. (2014). A parameter model of gas exchange for the seasonal sea ice zone. *Ocean Science*, *10*(1), 17–28. https://doi.org/10.5194/os-10-17-2014

Lu, P., Li, Z., Cheng, B., & Leppäranta, M. (2011). A parameterization of the ice-ocean drag coefficient. *Journal of Geophysical Research*, *116*(C7), 2010JC006878. https://doi.org/10.1029/2010JC006878

Lueck, R. G. (2015). Calculating the rate of dissipation of turbulent kinetic energy. Retrieved from http://rocklandscientific.com/?wpdmdl51034

MacKinnon, J. A., Simmons, H. L., Hargrove, J., Thomson, J., Peacock, T., Alford, M. H., et al. (2021). A warm jet in a cold ocean. *Nature Communications*, *12*(1), 2418. https://doi.org/10.1038/s41467-021-22505-5

Macoun, P., & Lueck, R. G. (2004). Modeling the spatial response of the airfoil shear probe using different sized probes. *Journal of Atmospheric and Oceanic Technology*, *21*(2), 284–297. https://doi.org/10.1175/1520-0426(2004)021<0284:mtsrot>2.0.co;2

McDougall, J., & Barker, P. (2011). *Getting started with TEOS-10 and the Gibbs Seawater (GSW) oceanographic toolbox*, SCOR/IAPSO WG127 (ISBN: 978-0-646-55621-5). 28.

McPhee, M. G. (1992). Turbulent heat flux in the upper ocean under sea ice. *Journal of Geophysical Research*, *97*(C4), 5365–5379. https://doi.org/10.1029/92jc00239

McPhee, M. G. (2002). Turbulent stress at the ice/ocean interface and bottom surface hydraulic roughness during the SHEBA drift. *Journal of Geophysical Research*, *107*(C10), 8037. https://doi.org/10.1029/2000JC000633

McPhee, M. G. (2008). *Air-ice-ocean interaction: Turbulent ocean boundary layer exchange processes*, Springer.

McPhee, M. G. (2017). The sea ice-ocean boundary layer. In D. N. Thomas (Ed.), *Sea ice* (pp. 138–159). John Wiley and Sons, Ltd.

McPhee, M. G., & Stanton, T. P. (1996). Turbulence in the statistically unstable oceanic boundary layer under Artic leads. *Journal of Geophysical Research*, *101*(C3), 6409–6428. https://doi.org/10.1029/95jc03842

Meier, W., Perovich, D., Farrell, S., Haas, C., Hendricks, S., Kaleschke, L., et al. (2021). Sea ice (in 'state of the climate in 2020'). *Bulletin America Meteorology Social*, *102*(8), S290–S292. https://doi.org/10.1175/BAMS-D-21-0086.1

Nasmyth, P. (1970). *Ocean turbulence (Unpublished doctoral dissertation)*, The University of British Columbia.

Nicolaus, M., Perovich, D. K., Spreen, G., Granskog, M. A., von Albedyll, L., Angelopoulos, M., et al. (2022). Overview of the MOSAiC expedition: Snow and sea ice. *Elementa*, *10*(1). https://doi.org/10.1525/elementa.2021.000046

Nixdorf, U., Dethloff, K., Rex, M., Shupe, M., Sommerfeld, A., Perovich, D. K., et al. (2021). MOSAiC extended acknowledgement. *Zenodo*, https://doi.org/10.5281/zenodo.5179739

Oakey, N. S. (1982). Determination of the rate of dissipation of turbulent energy from simultaneous temperature and velocity shear microstructure measurements. *Journal of Physical Oceanography*, *12*(3), 256–271. https://doi.org/10.1175/1520-0485(1982)012<0256:dotrod>2.0.co;2

Padman, L., Plueddemann, A. J., Muench, R. D., & Pinkel, R. (1992). Diurnal tides near the Yermak Plateau. *Journal of Geophysical Research*, *97*(C8), 12639–12652. https://doi.org/10.1029/92jc01097

Peralta-Ferriz, C., & Woodgate, R. A. (2015). Seasonal and interannual variability of pan-Arctic surface mixed layer properties from 1979 to 2012 from hydrographic data, and the dominance of stratification for multiyear mixed layer depth shoaling. *Progress in Oceanography*, *134*, 19–53. https://doi.org/10.1016/j.pocean.2014.12.005

Perlin, A., Moum, J. N., Klymak, J. M., Levine, M. D., Boyd, T., & Kosro, P. M. (2005). A modified law-of-the-wall applied to oceanic bottom boundary layers. *Journal of Geophysical Research*, *110*(C10), C10S10. https://doi.org/10.1029/2004JC002310

Peterson, A. K., Fer, I., McPhee, M. G., & Randelhoff, A. (2017). Turbulent heat and momentum fluxes in the upper ocean under Arctic sea ice. *Journal of Geophysical Research: Oceans*, *122*(3), 1–18. https://doi.org/10.1002/2016JC012283

Price, J. F., Baringer, M. O., Lueck, R. G., Johnson, I., andAmbar, G. C., Parilla, G., et al. (1993). Mediterranean outflow and mixing dynamics. *Science*, *259*(5099), 1277–1282. https://doi.org/10.1126/science.259.5099.1277

Rabe, B., Heuzé, C., Regnery, J., Aksenov, Y., Allerholt, J., Athanase, M., et al. (2022). Overview of the MOSAiC expedition: Physical oceanography. *Elementa: Science of the Anthropocene*, *10*(1). https://doi.org/10.1525/elementa.2021.00062

Schulz, K., Mohrholz, V., Fer, I., Janout, M., Hoppmann, M., Schaffer, J., & Koenig, Z. (2022a). A full year of turbulence measurements from a drift campaign in the Arctic Ocean 2019–2020. *Scientific Data*, *9*(1), 472. https://doi.org/10.1038/s41597-022-01574-1

Schulz, K., Mohrholz, V., Fer, I., Janout, M. A., Hoppmann, M., Schaffer, J., et al. (2022b). Turbulent microstructure profile (MSS) measurements from the MOSAiC drift, Arctic Ocean [dataset]. PANGAEA. Retrieved from https://doi.org/10.1594/PANGAEA.939816

Smith, M., & Thomson, J. (2019). Ocean surface turbulence in newly formed marginal ice zones. *Journal of Geophysical Research*, *124*(3), 1382–1398. https://doi.org/10.1029/2018JC014405

Stanton, T. P., Shaw, W. J., & Hutchings, J. K. (2012). Observational study of relationships between incoming radiation, open water fraction, and ocean-to-ice heat flux in the transpolar drift: 2002–2010. *Journal of Geophysical Research*, *117*(C7). https://doi.org/10.1029/2011JC007871

Steele, M., Morison, J. H., & Untersteiner, N. (1989). The partition of air-ice-ocean momentum exchange as a function of ice concentration, floe size, and draft. *Journal of Geophysical Research*, *94*(C9), 12739–12750. https://doi.org/10.1029/JC094iC09p12739

Zippel, S., & Thomson, J. (2016). Air-sea interactions in the marginal ice zone. *Elementa: Science of the Anthropocene*, *4*, 000095. https://doi.org/10.12952/journal.elementa.000095